



# NeuriTES. Monitoring neurite changes through transfer entropy and semantic segmentation in bright-field time-lapse microscopy

Arianna Mencattini, Alida Spalloni, Paola Casti, Maria Colomba Comes, Davide Di Giuseppe, Gianni Antonelli, Michele d'Orazio, Joanna Filippi, Francesca Corsi, Hervé Isambert, et al.

## ► To cite this version:

Arianna Mencattini, Alida Spalloni, Paola Casti, Maria Colomba Comes, Davide Di Giuseppe, et al.. NeuriTES. Monitoring neurite changes through transfer entropy and semantic segmentation in bright-field time-lapse microscopy. *Patterns*, 2021, 2 (6), pp.100261. 10.1016/j.patter.2021.100261 . hal-03451129

**HAL Id: hal-03451129**

**<https://hal.science/hal-03451129>**

Submitted on 26 Nov 2021

**HAL** is a multi-disciplinary open access archive for the deposit and dissemination of scientific research documents, whether they are published or not. The documents may come from teaching and research institutions in France or abroad, or from public or private research centers.

L'archive ouverte pluridisciplinaire **HAL**, est destinée au dépôt et à la diffusion de documents scientifiques de niveau recherche, publiés ou non, émanant des établissements d'enseignement et de recherche français ou étrangers, des laboratoires publics ou privés.

# Patterns

## NeuriTES. Monitoring neurite changes through transfer entropy and semantic segmentation in bright-field time-lapse microscopy

### Highlights

- Monitoring of cell phenotype changes by fluorescence label-free time-lapse microscopy
- Adaptive semantic segmentation for the robust detection of cell shape
- TE to correlate morphological and textural soma descriptors along time
- Directed TE graph for the representation of mutual relationship among descriptors

### Authors

Arianna Mencattini, Alida Spalloni, Paola Casti, ..., Corrado Di Natale, Patrizia Longone, Eugenio Martinelli

### Correspondence

[martinelli@ing.uniroma2.it](mailto:martinelli@ing.uniroma2.it)

### In brief

Nowadays, observational traits (phenotype) of biological entities complement with genomics offering the possibility to monitor phenomenon evolutions and underlying mechanism (neurodegeneration, cancer cell replication, etc.). By complementing video, data analysis, and machine learning approaches with label-free time-lapse microscopy, NeuriTES tool allows automatically analyzing such traits and extracting as outcomes proof of concepts and visual graph-based representation of the phenotypical rationale behind.



Article

# NeuriTES. Monitoring neurite changes through transfer entropy and semantic segmentation in bright-field time-lapse microscopy

Arianna Mencattini,<sup>1,2</sup> Alida Spalloni,<sup>3</sup> Paola Casti,<sup>1,2</sup> Maria Colomba Comes,<sup>1,2</sup> Davide Di Giuseppe,<sup>1,2</sup> Gianni Antonelli,<sup>1,2</sup> Michele D'Orazio,<sup>1,2</sup> Joanna Filippi,<sup>1,2</sup> Francesca Corsi,<sup>2</sup> Hervé Isambert,<sup>4</sup> Corrado Di Natale,<sup>1</sup> Patrizia Longone,<sup>3</sup> and Eugenio Martinelli<sup>1,2,5,\*</sup>

<sup>1</sup>Department of Electronic Engineering, University of Rome Tor Vergata, 00133 Rome, Italy

<sup>2</sup>Interdisciplinary Center for Advanced Studies on Lab-on-Chip and Organ-on-Chip Applications (ICLOC), University of Rome Tor Vergata, 00133 Rome, Italy

<sup>3</sup>Molecular Neurobiology Unit, Fondazione Santa Lucia-IRCCS, Via Ardeatina, 306/354, 00179 Rome, Italy

<sup>4</sup>Institut Curie - Centre de Recherche, CNRS-UMR168 11, rue P. et M. Curie, 75005 Paris, France

<sup>5</sup>Lead contact

\*Correspondence: [martinelli@ing.uniroma2.it](mailto:martinelli@ing.uniroma2.it)

<https://doi.org/10.1016/j.patter.2021.100261>

**THE BIGGER PICTURE** One of the most challenging frontiers for the automatic understanding of biological systems is fluorescent label-free imaging in which the behavior changes of living being are characterized without cell staining. To this aim, we present here the NeuriTES platform that revisits standard paradigms of video analysis to detect unlabeled objects and correlate the analysis to phenotype evolution of the mechanisms under observation. Through the exploitation of adaptive algorithms and of transfer entropy measures, the platform assures regular cell detection and the possibility to extract reliable parameters related to the evolving cell system. As a proof-of-concept, NeuriTES is applied to two fascinating phenotype investigation scenarios, amyotrophic lateral sclerosis (ALS) disease mechanism and the study of the effects of a chemotherapy drug on living prostate cancer cells (PC3) cultures. Directed graphs assist the biologists with a visual understanding of the mechanisms identified.



**Proof-of-Concept:** Data science output has been formulated, implemented, and tested for one domain/problem

## SUMMARY

One of the most challenging frontiers in biological systems understanding is fluorescent label-free imaging. We present here the NeuriTES platform that revisits the standard paradigms of video analysis to detect unlabeled objects and adapt to the dynamic evolution of the phenomenon under observation. Object segmentation is reformulated using robust algorithms to assure regular cell detection and transfer entropy measures are used to study the inter-relationship among the parameters related to the evolving system. We applied the NeuriTES platform to the automatic analysis of neurites degeneration in presence of amyotrophic lateral sclerosis (ALS) and to the study of the effects of a chemotherapy drug on living prostate cancer cells (PC3) cultures. Control cells have been considered in both the two cases study. Accuracy values of 93% and of 92% are achieved, respectively. NeuriTES not only represents a tool for investigation in fluorescent label-free images but demonstrates to be adaptable to individual needs.

## INTRODUCTION

Live-cell imaging has become a fundamental framework to better understand cellular processes and biological functions.<sup>1</sup> To enhance cells appearance, however, fluorescent labeling techniques are commonly used to increase the contrast of bright-field

images, to visualize proteins and subcellular compartments to help us answer biological questions and make new discoveries.<sup>2–5</sup> Unfortunately, labeling prevents several kinds of living cell analyses, due to its invasiveness, which may perturb the system under investigation or at least produce toxic effects, finally compromising research findings. A non-invasive and non-toxic



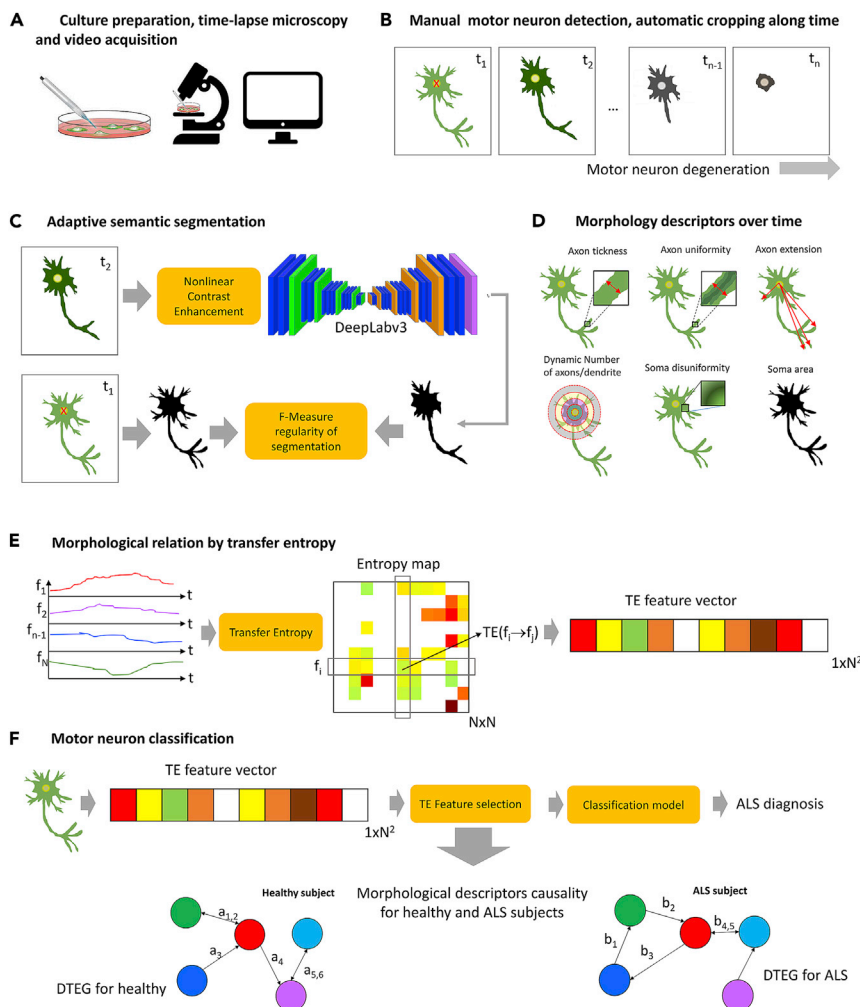


**Figure 1. A schematic view of the whole NeuriTES platform**

(A) Culture preparation and time-lapse microscopy acquisition.

(B) Manual detection and automatic cropping of motor neurons in each video sequence in the first frame.

(C) Application of the adaptive semantic segmentation-supervised approach for the automatic extraction of the motor neuron shape along the temporal evolution in the video.

(D) Extraction of the morphological descriptors from the shapes over time.

(E) The morphological descriptor signals are then processed through the multivariate transfer entropy (TE) operator for the extraction of the mutual relationship.

(F) The most relevant TE descriptors are then used as features vectors in motor neuron classification through standard classification models. The DTEG related to the comparative classes (healthy versus ALS samples) are then used for a further visual understanding of the neurite outgrowth processes.

Among diverse biological scenarios, one of the most challenging for LFI is represented by neuron cultures, due to the very complex architecture of neuronal cells (see a sketch in Figure 1B). Neuronal cells, and in particular motor neurons, are involved in a wide spectrum of neurodegenerative disorders, including amyotrophic lateral sclerosis (ALS), a fatal neurodegenerative disease characterized, as a hallmark trait, by the death of motor neurons in the motor cortex, brain stem, and spinal cord.<sup>7–14</sup> If, at the molecular level, numerous studies have demonstrated

alternative to fluorescent microscopy is fluorescent label-free imaging (LFI), in which combined contrast improving and image analysis algorithms are used to analyze cell culture without the need for cell staining. LFI can provide valuable biological information through analyzing cellular dynamics and morphology. Firstly, cells are being analyzed in their native, unperturbed state, leading to the extraction of more reliable and biologically relevant information. Secondly, it is much more fast and cheaper thanks to the possibility to use a standard light source avoiding any genetic modification or cell line generation.<sup>6</sup> Finally, the most important advantage is the duration of time-lapse experiments, which is not limited by phototoxicity. This opens the possibility to conduct dynamic modeling analysis in which the evolution of cell phenotype (i.e., cell morphology and behavior) can be correlated to cellular events, such as cell division, proliferation, motility, migration, differentiation, and death. However, LFI is still at a very early development stage due to the intrinsic difficulty in detecting objects of interest (cells, bacteria, etc.) or in easily differentiating cell types at very low optical contrast of images. A huge effort in image and video analysis is required to overcome such difficulty and to be able to extract objects of interests without the need for cell labeling.

how neurodegeneration proceeds in a dying-back manner from the distal to the proximal axon,<sup>15–19</sup> investigation of the phenotype aspects of the degradations are still in their infancy. In this context, identification and assessment of neurite outgrowth and dendritic development can represent important readouts in experiments involved in the understanding of the degeneration mechanisms of ALS.

Due to the very high complexity in motor neuron structure and temporal degradation processes, state-of-the-art methods for the analysis of living motor neuron in culture are based on cell-staining techniques.<sup>20–28</sup> If on one hand, cell labeling allows the user to easily segment the soma and the neurites from the background and further analyze their morphological evolution, according to the limitations highlighted above, the construction of a dynamic modeling of the degradation process of neurites is prevented, and most of the existing tools end up providing only an improved view of the neuronal cell<sup>21</sup> or at most a few static measurements at time points of a few hours.<sup>20,23</sup> The high costs and the toxicity effects hinder the possibility to conduct massive analysis for long observation times (days) at a very high frame rate (minutes) with the immediate consequences of losing information on the dynamics of the process

underlying neurite outgrowth and degradation, along with the possibility to correlate their mutual relationship. To provide an overview of the existing approaches, Table 1 lists all the available tools for investigation of neurite evolution, highlighting imaging modalities, the kind of measurements allowed, and the amount of user intervention. It can be noted that, except for NeuriteSegmentation,<sup>20</sup> the remaining tools have been applied on labeled images or on high-contrast-imaging modalities.<sup>23</sup> As a consequence, none of the tools allows dynamic modeling of the outgrowth process and only two of them present discriminant analysis via statistical tests performed on one<sup>20</sup> or a very few individual shape descriptors.<sup>28</sup>

In this work, we present a novel software architecture, called NeuriTES, which works automatically in FLI sequences of living motor neuron cultures. The main strength of NeuriTES is to conjugate unlabeled bright-field images and time-lapse microscopy (frame rate in the order of minutes) with high performing image analysis and dynamic feature extraction tools. NeuriTES provides the user with: (1) a very accurate automatic segmentation of each motor neuron cell moving along the sequence, thanks to an adaptive deep learning<sup>29</sup> semantic segmentation (SS) strategy; (2) a series of morphological and textural soma and neurite temporal descriptors along with their mutual relationship through the implementation of the transfer entropy (TE)<sup>30</sup> paradigm; (3) a directed graph of the mutual relationships identified among the descriptors under specific comparative biological conditions (i.e., disease versus healthy, different time of growth) that may assist the biologist with a visual understanding of the mechanisms related to, for example, neurodegenerative disease, such as ALS.

The main assumption underlying NeuriTES is the need for algorithm adaptation to avoid continuous user intervention<sup>21–25</sup> and manually modified algorithm parameters.<sup>20,26–28</sup> For this reason, we introduce in NeuriTES, an adaptive mechanism that allows more regular and reliable segmentation results along the image sequence of the same motor neuron. To this aim, we introduce the so-called adaptive semantic segmentation (ASS) technique that conjugates pretrained segmentation networks and perturbative contrast analysis of the frames under consideration to increase the regularity of the segmentation result.

In addition to the ASS novel paradigm, we also include in NeuriTES a very powerful analysis technique based on the TE paradigm. TE allows to mutually correlate the diverse descriptors extracted from the same cell along time and estimate their mutual temporal relationship. This information allows the user to establish a sort of leader/follower relationship among the time-varying variables (e.g., shortening versus flattening of neurites along the degenerative process) for further understanding of the outgrowth process. TE information can be also used as indicative of the degeneration process. The powerfulness of the TE strategy is strengthened by the possibility to associate to the resulting matrix (i.e., the matrix containing the TE between descriptors  $i$  and  $j$ ) a directed graph. Such a graph, later called the disease transfer entropy graph (DTEG), visually indicates which relationships are relevant in the model of a particular biological condition (e.g., ALS disease) and which are standardly present in the neurite outgrowth process of healthy motor neurons. In this way, biologists may further differentiate the physiological motor neuron aging process from pathological conditions.

We believe that the strategies involved in NeuriTES, going from ASS, to TE and related disease graph representation, are totally general and may offer to data scientists hints for improving dynamic system understanding, monitoring, and control. For the sake of demonstrating this generalizability, we also apply the NeuriTES tool to a very different case study of living prostate cancer cell cultures<sup>31</sup> treated with a chemotherapeutic drug. We export graphs for the two case studies.

To conclude, the present tool tries to establish a bridge between biologists and data scientists, combining minimally invasive imaging techniques, such as label-free bright-field time-lapse microscopy with more recent image and data analysis algorithms, and dynamical modeling.

## RESULTS

### A sketch of NeuriTES platform

To introduce the reader to the main steps involved in the NeuriTES platform, Figure 1 shows a sketch of the whole platform, exemplified over motor neuron investigation. First, a mixed spinal cord culture, containing motor neurons, is prepared and cultured in a Petri dish. Then, a video is acquired over 1 day at 1 frame/min (1,440 frames per video) (Figure 1A). A crop of each motor neuron is manually extracted in the first frame of each video by looking for a large cell body, long axon, extensive dendritic Arborization, and by a minimum threshold diameter criterion ( $>30\ \mu\text{m}$ ).<sup>32,33</sup> A video for each motor neuron lasting 1 day is then extracted (Figure 1B). Examples of a full field-of-view frame acquired by time-lapse microscopy is shown in the supplemental figures: *Frame\_1\_WT\_8<sup>th</sup>\_day.tif* and *Frame\_1\_WT\_8<sup>th</sup>\_day\_marked.tif*. Each motor neuron is then automatically segmented (Figure 1C). Image segmentation is a general framework for automatic object characterization aimed at automatically identifying pixels belonging to the object of interest. There exist many approaches for automatic segmentation based on various criteria related to pixel similarity as well as to local pixel intensity changes.<sup>34</sup> Among various methods, supervised approaches, such as SS, demonstrated to be the most effective methodologies.<sup>29</sup> In this work, SS based on a pretrained convolutional neuronal network (CNN),<sup>35</sup> i.e., ResNET50,<sup>36</sup> has been used to segment motor neuron in all the frames of each video, starting from a small subset (less than 1%) of manually segmented motor neuron provided by the biologists in the first frame of a subset of videos. The segmentation regularity is achieved by perturbing the nonlinear contrast of the actual frame so to maximize the similarity measure of actual and previous segmentation results. This new approach is referred as ASS (Figure 1C). Morphological descriptors (Figure 1D) related to the neurite thickness, flatness, extension, and general motor neuron appearance in terms of luminance inhomogeneity, and automatic implementation of the Sholl analysis of neurites<sup>37</sup> are then extracted along the segmented sequence of each motor neuron. Each descriptor is further coded in terms of its statistics over the different boundary points of the motor neuron mask or of the internal soma (e.g., standard deviation values of the neurite thickness over all the boundary points of the segmented neuron). The obtained descriptors acquired in each frame can be used as indicators of degeneration over time to improve the discriminant capability of the platform. In addition, in NeuriTES, it is assumed that the relationship among the descriptors can be more

**Table 1. Available tools for digital investigation of neurite evolution**

Method Name	Microscopy technique	Segmentation technique	Image processing	Measurement achieved	Dynamic analysis	Discriminative task
NeuriteSegmentation <sup>20</sup>	bright field	automatic	local adaptive thresholding and manual refining of the artifacts	axon area, average and maximal axon length	yes, time points at 24 h, 48 h, 5 days, 8 days, 14 days	statistical test
Neuron-J <sup>21</sup>	fluorescence	semi-automatic	minimum detection and tracing algorithm; second-order difference filters	neurite intersection and occupied area	no	no
NeuriteTracer <sup>22</sup>	fluorescence	semi-automatic	thresholding and skeletonization	neurite length, quantity of soma	no	no
NeuronGrowth <sup>23</sup>	phase contrast, differential interference contrast, fluorescence	semi-automatic	sequence alignment, background subtraction, flat field correction, light normalization, cropping, DIC correction, livewire and snakes algorithm	neurite length	yes, rate of 2–12 min per image for several days	no
NeuronMetrics <sup>24</sup>	fluorescence	semi-automatic	contrast improvement, skeletonization, Laplacian	primary neurite count, neurite length, branch number, quantity of soma, soma's size	no	no
NeurphologyJ <sup>25</sup>	fluorescence	semi-automatic	image enhancement, background subtraction, edge detection and binarization, morphological operations, skeletonization, arithmetic and logical operations	neurite length, branch number, quantity of soma, soma's size	no	no
Neurite-IQ <sup>26</sup>	fluorescence	automatic	dynamic programming	neurite length	no	no
NeuronCyto_II <sup>27</sup>	fluorescence	automatic	background removal, matrix-forest theorem on directed graph	axonal length, branching, complexity, crossover	no	no
Neurite-J <sup>28</sup>	fluorescence	automatic	global thresholding	neurite length and arbor area, circularity and explant body area	no	statistical test
NeuriTES	bright field	automatic	adaptive semantic segmentation (deep learning, adaptive contrast enhancement)	neurites' length, diameter, number of primary axons, neurites' flatness, soma aspects and area, and their temporal evolution, TE analysis	yes, rate of 1 min per image for 6 h to 1 day	statistical test and linear discriminant analysis classifier

The main details of the state-of-the-art approaches are indicated.



**Table 2. Video data description**

VIDEO data description								
No. of videos available 79 (21,646 frames)	no. of videos at 6 <sup>th</sup> day50				no. of videos at 8 <sup>th</sup> day29			
No. of labeled 15 (150 frames)	no. of labeled videos2		no. of unlabeled videos48		no. of labeled videos13		no. of unlabeled videos16	
No. of unlabeled 64 (21,496 frames)								
G93A 51 (13,974 frames)	G93A2	WT0	G93A37	WT11	G93A6	WT7	G93A6	WT10
Wild-type 28 (7,672 frames)								
The numbers of videos of each motor neuron for different days of acquisition, labeled and unlabeled cases, and presence of the disease are listed								

The numbers of videos of each motor neuron for different days of acquisition, labeled and unlabeled cases, and presence of the disease are listed.

informative than the descriptors themselves. The TE operator maps such a relationship into an asymmetric entropy map (each element quantifies the information transfer from descriptor  $i$  to the descriptor  $j$ , Figure 1E), which is considered as a new feature vector for classification (Figure 1F). After feature selection, the selected TE values provides the most relevant relationships among morphological descriptors that can be also used to construct the so-called DTEG,<sup>38</sup> as shown in Figure 1F.

In particular, the DTEG is a graph (one for each category of subjects) representing a visual cue of the disease in terms of significant morphological relationships along with a weight attributed to this relationship provided by the TE value. In this way, the biologist is not only provided with a black box platform for the automatic monitoring of motor neuron degeneration but also with a visual representation of the mechanism and of their biological implication (e.g., motor neuron body roughness implies neurite flatness in ALS samples).

## CASE study 1

### Source data

In this study we used primary spinal cord cultures prepared from transgenic G1H mice, which overexpress a mutant human SOD1 gene containing a glycine93→alanine (G93A) substitution. These mice have been extensively validated as an animal model of ALS due to the development of symptoms and a motor neuron pathology that mimics those found in ALS patients.<sup>39</sup> We acquired videos of motor neurons from two distinct kind of cells, G93A and wild-type (WT), as control. The original videos were acquired using time-lapse microscopy at a frame rate of 1 frame/min over a day at the 6<sup>th</sup> and 8<sup>th</sup> days *in vitro*. Based on the focus and illumination conditions obtained during time-lapse microscopy acquisitions an expert biologist manually segmented 15 motor neurons at the initial frame using ImageJ.<sup>40</sup> To increase the training set for segmentation, we transfer the same ground truth images also to the corresponding next 9 frames (10 min in total), leading to 10 consecutive labeled frames. The assumption is that the motor neurons' motility is almost null within 10 min of observation and that the same ground truth (GT) image can be assumed as the truth segmentation for the subsequent frames. A total number of 150 labeled frames (15 motor neurons by 10 labeled frames) were then used to train the SS network and to assess the segmentation performance also

with respect to comparative approaches. Such setting also allowed us to reduce the memory storage of the entire video sequence (see Table 3).

The analyzed motor neurons derive from a total of nine distinct cultures. In addition, an expert located the center of additional motor neurons to increase the dataset for analysis. According to the coordinates provided, each motor neuron was then automatically cropped and a distinct video was extracted from each motoneuron progression.

Table 2, lists the number of videos for each condition either in terms of day of acquisition (6<sup>th</sup> or 8<sup>th</sup>) and in terms of the presence of the disease phenotype (WT versus G93A). In addition, we also detailed the number of videos with labeled and unlabeled cells. Videos *Supplementary\_video\_G93A\_6<sup>th</sup>\_day.avi*, *Supplementary\_video\_G93A\_8<sup>th</sup>\_day.avi*, *Supplementary\_video\_WT\_6<sup>th</sup>\_day.avi*, and *Supplementary\_video\_WT\_8<sup>th</sup>\_day.avi* provide four examples of videos for WT and G93A motor neurons, acquired on the 6<sup>th</sup> and 8<sup>th</sup> days, respectively (see data and code availability for the link to download the videos).

### Performance of ASS using labeled images

Regarding the assessment of the ASS network, we calculated the performance of the network in training where we had GT images, namely images for which an expert biologist draws the shape of the motor neuron, as mentioned above. Performance was evaluated in terms of standard metrics, such as recall ( $R$ ), precision ( $P$ ), and  $F$  measure ( $FM$ ) (i.e., the harmonic mean of  $R$  and  $P$ ),<sup>41</sup> hereafter defined. Denoting by true positive ( $TP$ ) those pixels correctly assigned to the motor neuron neurites, false positive ( $FP$ ) those pixels assigned to the motor neuron neurites but originally belonging to the background culture, and false negative ( $FN$ ) those pixels belonging to the motor neuron neurites but missed by the algorithm, we had

$$R = \frac{TP}{TP + FN}, \quad P = \frac{TP}{TP + FP}, \quad FM = \frac{2 \cdot CM \cdot CR}{CM + CR}. \quad (\text{Equation 1})$$

$R$  is affected by under-segmentation where the segmentation algorithm misses some parts of the motor neurons.  $P$  is affected by over-segmentation in which the segmentation is overcomplete with a relevant number of FPs.  $FM$  is a combination of the two metrics and account for both kind of segmentation errors. The value of 2 in the  $FM$  definition represents a normalization factor to assure  $FM$  is in the range [0,1].

**Table 3. Total overhead**

Single motor neuron video (274 frames)	Computational time (s)	Memory storage (double precision) (kB)
Adaptive semantic segmentation (no training)	~750	~10,000
Feature extraction	~1,150	~50
TE computation	~2	~5
Total overhead	~1,902	~10,055

Computational overhead and memory storage for the analysis of a single motor neurons.

Figure 2A shows four examples of motor neuron segmentation results obtained by ASS for WT and G93A samples from the 6<sup>th</sup>-day and 8<sup>th</sup>-day experiments. Figure 2B shows the boxplots of  $R$ ,  $P$ , and  $FM$  separately calculated for the 6<sup>th</sup> and 8<sup>th</sup> days. It can be noted that, in general, the SS results are overcomplete, leading to a very high  $R$  value (on average larger than 0.95) and a smaller  $P$  value (on average 0.25). In addition, it is important to note that the above metrics do not account necessarily for shape similarity between the GT and the segmented shape. In particular, in some cases, see comparative results below, an overcomplete result conjugated with a moderated precision value, may still convey the needed information for further morphological characterization, which is the scope of our analysis.

#### Performance of ASS with respect to standard SS

ASS allows to increase the overall robustness of the segmentation step. Standardly, the SS procedure in a frame does not take into account the SS relative to the previous frame, leading to unexpected segmentation results in certain frames due, for example, to changes in illumination or in the image focus. To address such a problem, it was necessary to modify the standard approach to confer more regularity to the segmentation in each frame. Regularity is fundamental to obtain more stable morphological descriptors with regular temporal trend. Figure 2C shows the boxplot of the  $FM$  calculated considering the segmentation of two consecutive frames at a time (i.e., the  $FM$  in this case is used as a measure of regularity of the shape segmented over time). The adaptive and the standard SS are also visually compared for a WT motor neuron recorded at the 8<sup>th</sup> day. Results are shown in Figure 2D. Note that, in general, the SS results for the two comparative approaches are similar, because, for computational complexity constraints, the adaptive approach is used only when the  $FM$  between consecutive frames is lower than 0.8 to avoid applying useless laborious procedures when the two segmentation results are already similar. However, it can be noted that  $FM$  using the adaptive approach is always larger or equal to that obtained using the standard method, leading to more regular results. In addition, from Figure 2D it can be observed that the standard SS strategy produces some unwanted protrusions that may alter the morphological assessment of the motor neuron shape (see, for example, the first, second, and fifth frames).

#### Individual discrimination ability of morphological descriptors

Each segmented shape along with the corresponding bright-field frame are processed for the extraction of 21 morphological descriptors (see the experimental procedures) over an observation time of 1 day (6<sup>th</sup> or 8<sup>th</sup>). Each descriptor produces a time series of length 274 frames for each motor neuron, at a frame rate of 0.2 frame/min. The statistical signif-

icance of the descriptors extracted was assessed through the calculation of an individual discriminant power ( $DP$ ) for a generic descriptor  $f_i$  obtained as

$$DP(f_i) = \max(AUC(f_i), 1 - AUC(f_i))$$

where AUC represents the area under the ROC curve, which accounts for the general capability of discrimination of the descriptors with respect to a binary classification problem.<sup>42</sup> In this paper, the problem was the discrimination between healthy (WT) and unhealthy (G93A) motor neurons in mice cultures. Figure 3A shows the  $DP$  values for descriptors extracted from motor neurons visualized at the 6<sup>th</sup> day (x axis) and at the 8<sup>th</sup> day (y axis), respectively. For the sake of interpretability, we report in color only descriptors with a  $DP$  value higher than 0.75. The gray spots indicate the remaining feature values.

From Figure 3A it can be noted that only three descriptors, namely  $f_5$ ,  $f_7$ , and  $f_{17}$ , exceed the 0.75 minimum area (the purple rectangular region). Moreover, only two of them are discriminant for the 6<sup>th</sup>-day experiment ( $f_5$ ,  $f_{17}$ ). Such a low  $DP$  value represents a serious bottleneck for a high-performing monitoring system. In conclusion, out of the 21 descriptors, 14 have a  $DP$  lower than 0.6 making it prohibitive to construct a classification model using such features.

#### Discrimination ability of TE descriptors

As mentioned before, each descriptor is represented by a time series that depicts the trend of the descriptor over time during 1-day observations. The random contribution to the series is related to the acquisition process and to the electronic noise term induced by the platform for the analysis (quantization noise, photon noise, etc.) The temporal evolution of such a system may be quantified by the concept of Shannon's entropy.<sup>43</sup> For a system consisting of more than one component (time series in the following), such as the one presented in this work, important information on the structure of the observed phenomenon, i.e., morphological evolution, can be obtained by measuring to what extent the individual time series contributes to produce information and at what rate they exchange information among each other. The translated aspect is to what extent descriptors mutually increase the knowledge about the process by accounting for dynamical and directional information. The answer to this question is provided by the so-called multivariate TE (MUTE).<sup>30,43</sup> Entropy estimators are able to reveal the information transferred among variables represented by time series that, in our application, are represented by the morphological descriptors signals over time. More specifically, without the need to assume any particular probability distribution for the involved time series,



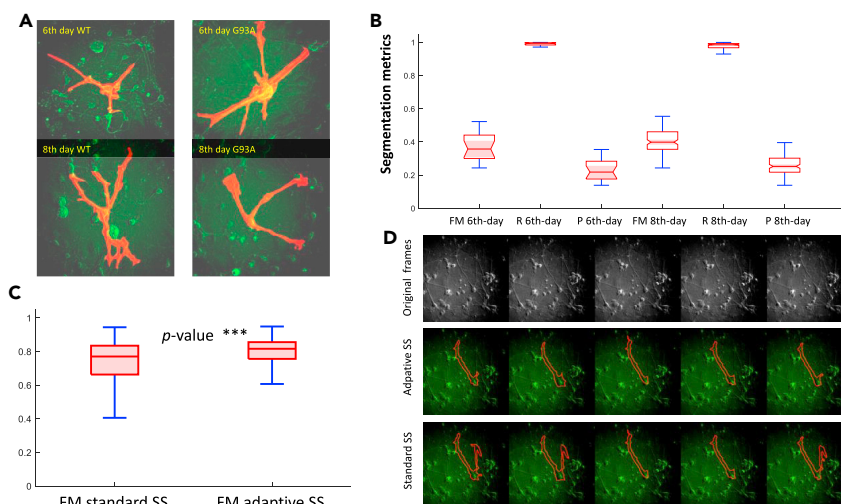


**Figure 2. Examples of ASS results**

(A) Four examples of segmentation results obtained with ASS (orange shapes) over-imposed on the original motor neuron crops: WT and G93A acquired at the 6<sup>th</sup> and 8<sup>th</sup> days.

(B) *FM*, *R*, and *P* distribution values calculated for all the ASS results relative to motor neurons with an available GT image, at 6<sup>th</sup> and 8<sup>th</sup> days.

(C) Comparison of the distribution of the *FM* values computed comparing the standard SS (left) and the ASS (right): the p values of the t test conducted to verify the significance of the difference are also indicated.

(D) An example of the visual effect of applying the ASS (second row) compared with the standard SS (third row) for a G93A motor neuron acquired on the 8<sup>th</sup> day.

with term TE we refer to the “predictive information transfer” intended as the amount of information added by the past (and present) states of a source time series to the present state of a target time series. Further mathematical details can be found in the [experimental procedures](#). The MUTE matrix consists of  $21 \times 21$  elements, each identifying the directed relationship between two descriptors conditioned to the remaining 19, except for the 21 diagonal elements that are forced to zero. Recalling the intrinsic asymmetry of the MUTE matrix due to the directionality of the descriptor relationship, we collected all the 420 TE descriptors of the MUTE matrix in a vector and treated them as descriptors. We denoted them as TE descriptors, or TE feature (TE-fs). To verify the significance of the TE-f, we calculated the *DP* values for the TE descriptors. The results are plotted in [Figure 3B](#) for the 6<sup>th</sup>-day (x axis) and 8<sup>th</sup>-day (y axis) cases, respectively. By using the same limit values (only for the sake of visualization) as in the case of morphological descriptors, it can be noted that even eight TE-fs have a *DP* score higher than 0.75 for the 8<sup>th</sup>-day experiment and even 11 TE-fs have a *DP* score higher than 0.75 in the 6<sup>th</sup>-day experiment. In addition, gray markers, 65 and 69 TE-fs have a *DP* score higher than 0.65 for the 6<sup>th</sup>-day and 8<sup>th</sup>-day experiments, respectively. This result confirms the fact that a high number of TE-fs can be used to construct a reliable classification model for both temporal scenarios. It is impor-

tant to note that, in general, the TE-fs selected are different for the two experimental scenarios (i.e., 6<sup>th</sup> and 8<sup>th</sup> days) giving evidence to the fact that timing plays a crucial role in the cell behavior also in relation to the degeneration of the neurite outgrowth. In addition, the TE-fs allow accounting for mutual information between descriptors over time rather than to the individual feature values. In light of this, the system is more robust to the dependence of the descriptor values on image focus and illumination conditions and related unexpected changes. This statement is further supported in the Discussion.

### Performance of automatic recognition of motor neurons with ALS (G93A) or WT

To demonstrate the effectiveness of the proposed monitoring platform, we designed two kinds of experiments. In the first one, we considered only motor neurons visualized on the 6<sup>th</sup> day and, in a second step, we selected motor neurons visualized on the 8<sup>th</sup> day. In each test, we implemented a leave-one-motor neuron-out (LOMO) cross-validation approach. The classification model is, in turn, trained on all the motor neurons except for the one left out and tested on that motor neuron. The procedure is repeated for all the motor neurons. Under the assumption that not all frames fully manifest the degradation effects, either because neurite degradation is a continuous ongoing process or because of the acquisition

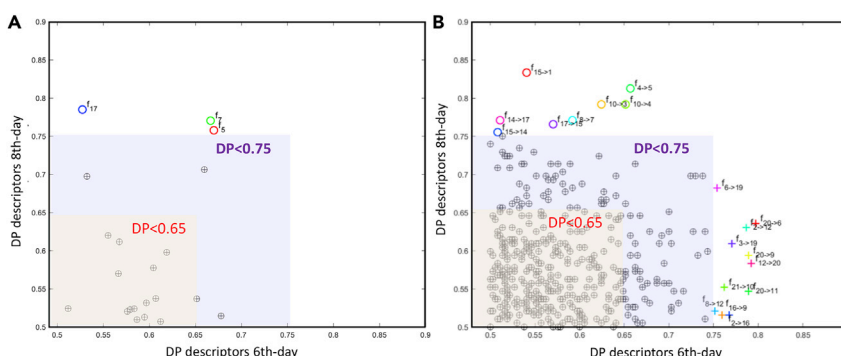


**Figure 3. Discriminant power score plot for standard morphological descriptors**

(A) versus TE descriptors (B). The gray boxes locate descriptors with a discriminant power (*DP*) lower than 0.65, the purple boxes locate descriptors with a *DP* smaller than 0.75 (and larger than 0.65). (A) Features with *DP* larger than 0.75 are indicated using their symbol, whereas (B) descriptors are indicated using the TE relationship associated. Circle markers relate to the 8<sup>th</sup> day and cross markers relate to the 6<sup>th</sup> day.

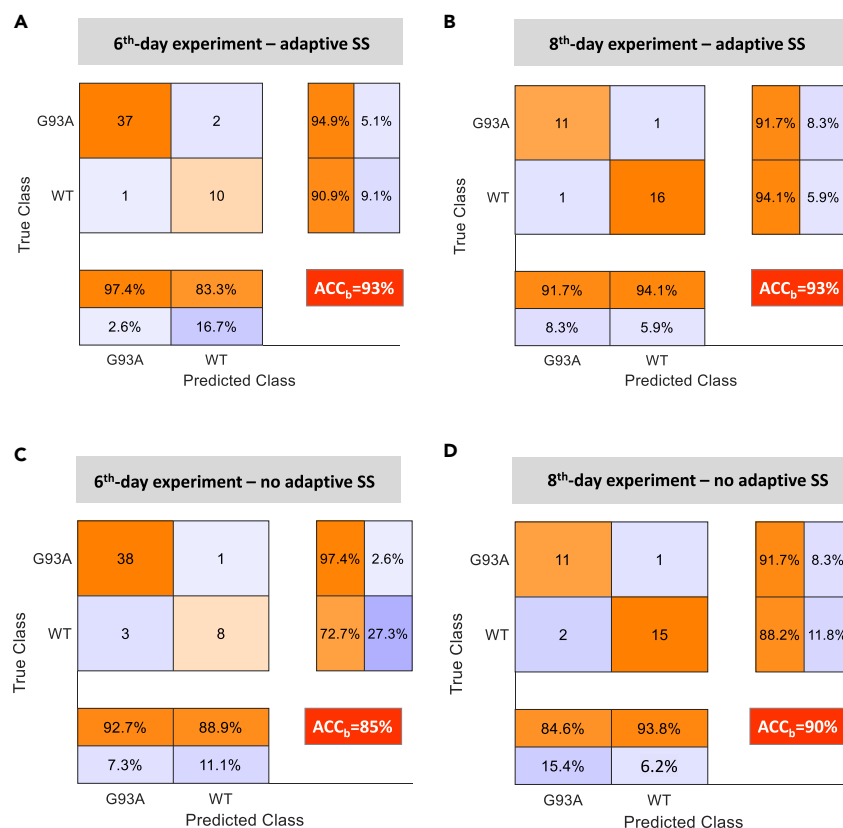


**Figure 4. Confusion matrices of competing approaches**

(A) Sixth-day experiment, ASS.  
(B) Eighth-day experiment, ASS.  
(C) Eighth-day experiment, SS.  
(D) Eighth-day experiment, SS.

of the 50 motor neurons observed on the 6<sup>th</sup> day, 39 were G93A and 11 were WT. The system achieved a final balanced accuracy value ACC<sub>b</sub> equal to 93%. Two G93A motor neurons were misclassified as WT and only one WT motor neuron was misclassified as G93A. Figure 4B shows the confusion matrix of the classification results related to the 8<sup>th</sup>-day experiment. Out of the 29 motor neurons observed on the 8<sup>th</sup> day, 12 were G93A and 17 were WT. The system achieved a final balanced accuracy value ACC<sub>b</sub> equal to 93%. Only one motor neuron G93A was misclassified as WT and only one WT motor neuron was misclassified as G93A, implementing the standard SS approach with no adaptation step. It can be noted that accuracy values worsen remarkably, especially on the 6<sup>th</sup>-day experiment. This is probably due also to the fact that the number of expert-segmented motor neurons on the 6<sup>th</sup> day is very low and the segmentation step is

more critical than that performed on the 8<sup>th</sup> day. In addition, the regularity offered by the adaptation assures an increasing reliability of the descriptors and consequently of the TE-fs extracted.

**Classification results for motor neurons visualized on the 6<sup>th</sup> and 8<sup>th</sup> days using standard SS**

Figures 4C and 4D shows the confusion matrices of the classification results obtained on the 6<sup>th</sup> and 8<sup>th</sup> days by the ASS (Figures 4A and 4B) approach compared with those achieved by standard SS (Figures 4C and 4D).

#### Classification results for motor neurons visualized on the 6<sup>th</sup> day and 8<sup>th</sup> day using ASS

Figure 4A shows the confusion matrices of the classification results related to the 6<sup>th</sup>-day experiment, using the described method. The true class indicates the expected class while predicted class represents the labels assigned by the classification model. Out

of the 50 motor neurons observed on the 6<sup>th</sup> day, 39 were G93A and 11 were WT. The system achieved a final balanced accuracy value ACC<sub>b</sub> equal to 93%. Two G93A motor neurons were misclassified as WT and only one WT motor neuron was misclassified as G93A. Figure 4B shows the confusion matrix of the classification results related to the 8<sup>th</sup>-day experiment. Out of the 29 motor neurons observed on the 8<sup>th</sup> day, 12 were G93A and 17 were WT. The system achieved a final balanced accuracy value ACC<sub>b</sub> equal to 93%. Only one motor neuron G93A was misclassified as WT and only one WT motor neuron was misclassified as G93A, implementing the standard SS approach with no adaptation step. It can be noted that accuracy values worsen remarkably, especially on the 6<sup>th</sup>-day experiment. This is probably due also to the fact that the number of expert-segmented motor neurons on the 6<sup>th</sup> day is very low and the segmentation step is

#### Case study 2

##### Source data

In this case study, we considered prostate cancer cells (PC3)<sup>31</sup> treated with a chemotherapeutic drug (etoposide). Etoposide, inhibiting the action of topoisomerase II, thus impairing the ligation step of the cell cycle, has a replication blocking effect over cancer cells. The aim of the study was to demonstrate that the mutual evolution of shape and texture descriptors of cells is indicative of the phenotype changes in PC3 treated with etoposide versus untreated cells. For this task, we considered the experimental setup described in Giuseppe et al.,<sup>31</sup> and applying NeurITES modules to label-free time-lapse microscopy video sequences of living PC3 cultured in a Petri dish (1 frame/min, 0.33 μm/pixel). The steps described in Figure 1 are sequentially applied to the analysis of PC3. Since there are a few small cells in a single frame, cells are first automatically tracked using the software Cell-Hunter as described in Giuseppe et al.<sup>31</sup> A region of interest

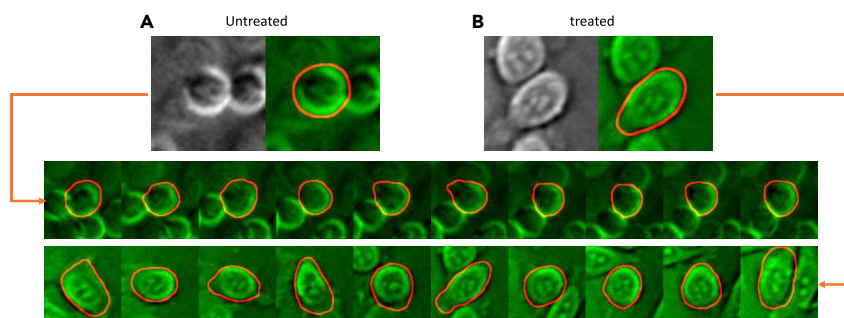


**Figure 5. Examples of ASS results for the PC3 cells**

(A) Untreated cell and (B) treated cell.

(ROI) is then extracted for each cell along its trajectory over time, thus leading to a sequence of ROIs for each moving cell. For the training of the SS network, a total of 24 cells (12 from control and 12 from treated cells) were manually segmented at the first frame. A total of 5,000 cell frames were extracted.

### Results in the automatic recognition of the effect of chemotherapy on PC3 phenotype

The 5,000 cell frames were automatically segmented by ASS after a dedicated SS network was trained over the first manually segmented frames of each track. On average, trajectories were 6 h long (360 values at a frame rate of 1 frame/min). Therefore, the shape a cell has in the first frame is totally independent from the shape after many hours. Figure 5 shows an example of segmented cell for an untreated cell (Figure 5A) and a treated cell (Figure 5B). Only some selected frames are visualized. Note that segmentation is still very challenging due to the changes in shape during the cell's movement and the closer cells in the surroundings.

Descriptors used for the task of classification are divided into three groups: first group  $f_{g1}$  includes five shape descriptors; the second group  $f_{g2}$  includes five texture descriptors related to the PC3 pixel intensity; the third group  $f_{g3}$  comprises four texture Haralick descriptors.<sup>44</sup> A total of 14 descriptors are used to characterize the cell along time. Further details on the descriptors are included in the experimental procedures. After TE estimation, 182 TE descriptors are used for the classification task. Accuracy of classification achieved implementing one-track-out cross-validation is about 92%. Figure 6 shows the confusion matrix associated to the experiment. Note that untreated cells were all correctly recognized, whereas only two treated cells were misrecognized as untreated.

## DISCUSSION

### Disease graphs for WT and G93A motor neurons

The TE descriptors selected for the scope of classification represent direct relationships between time-varying morphological characteristics of motor neurons, highlighting the potential of any mutual variation in neurite outgrowth than can be meaningful for the overall understanding of the motor neuron degeneration process due to the presence of an ALS-related mutation. To this end, we have evaluated the alterations caused by the overexpression in mouse motor neurons of the human SOD1 gene carrying the ALS-linked mutation at position 93 (G93A). A fascinating way to visually

represent such a relationships can be the use of DTEG. The DTEG tool allows the user to have a direct visual sketch of how the different aspects of the degeneration (i.e., alteration on general aspects,  $f_{17}$ – $f_{20}$ , alteration of neurites thickness and flatness,  $f_1$ – $f_4$  and  $f_5$ – $f_8$ , respectively, or finally alterations in heterogeneous and global neurite extension and numerosity,  $f_9$ – $f_{12}$ ,  $f_{21}$ , and  $f_{13}$ – $f_{16}$ , respectively) are related to the presence of ALS disease (of the ALS mutation). After a restricted number of TE-fs are selected (those having *DP* values higher than 0.75, see Figures 3A and 3B), we constructed the DTEG. The DTEG contains as many nodes as the number of individual descriptors involved in at least one selected mutual relationship and as many edges as the non-zero entries of the MUTE matrix for the TE-f selected. As an example, if the TE-f  $f_{i \rightarrow j}$  is selected, then the DTEG will contain the nodes *i* and *j* and the edge *i*–*j*. The direction of the edge is related to the fact that in the average MUTE matrix, calculated by averaging the MUTE matrices of a selected group of subjects (e.g., all the WT), the element in row *i* and column *j* is non-zero, and the weight of that edge is the average value of the MUTE matrix in position (*i*,*j*). Calculating a separate DTEG for WT and for G93A subjects for the 6<sup>th</sup> and 8<sup>th</sup> days, respectively, we are able to visually represent the overall relationship of descriptors extracted over healthy (WT) and unhealthy (G93A) subjects. To provide the reader with this further tool, we show in Figures 7A and 7B, the DTEGs for WT and G93A from the 6<sup>th</sup> day (Figure 7A) and 8<sup>th</sup> day (Figure 7B), respectively. We assigned the same color to the same feature group to simplify the interpretation, as indicated in the legend. The solid black edges identify the subgraphs that are in common for the two conditions (WT versus G93A). Conversely, for each category of subjects, the dashed orange edges identify the subgraphs additionally present and related to the specific condition (i.e., left, WT; right, G93A). The dashed orange circles also identify nodes that are also specific for each group of subjects, due to the addition of at least one more edge. For example, considering Figure 7A, we can observe that the presence of ALS disease (the ALS-related mutation) strongly reformulated the DTEG structure by not only including additional crucial nodes ( $f_{12}$ ) but also their relationship with many newly inserted nodes ( $f_{14}$ ) and already present nodes ( $f_8$ ,  $f_{20}$ , and  $f_{18}$ ), leading to a four-degree level for the additional node  $f_{12}$  (the degree level is the total number of incoming or outgoing edges).

Considering that  $f_{12}$  identifies the minimum distance of the neurite extremes, the additional subgraph related to the G93A subjects mainly establishes a relationship of  $f_{12}$  with motor neuron pixel intensity ( $f_{18}$  and  $f_{20}$ ), highlighting the fact that the degeneration in neurite outgrowth also implies an alteration in neurite appearance (entropy and standard deviation of the neurite soma,  $f_{18}$  and  $f_{20}$ , respectively). Such a

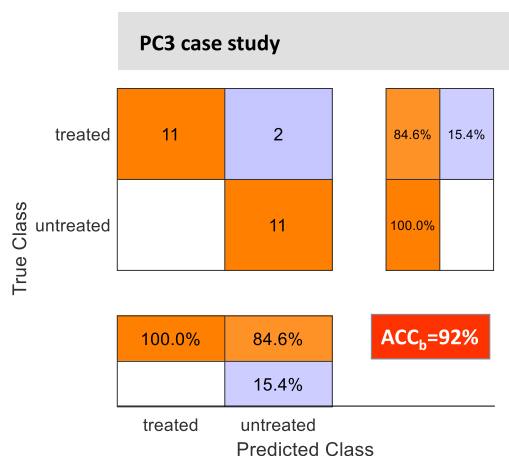


**Figure 6. Confusion matrices of PC3 experiment**  
Treated versus untreated cells.

relationship is not relevant in healthy MNs, as indicated by the absence of the node  $f_{12}$ . By considering Figure 7B, we can observe that the topology of the graph is totally different, indicating once more that timing plays a crucial role in the understanding of the degeneration process. First of all, the difference between healthy and unhealthy subjects in the topology of the two graphs is less evident than in the 6<sup>th</sup>-day experiment. More specifically, node  $f_{15}$  assumes a relevance as it turns from a two-degree node into a seven-degree node. The new connections are also related to the addition of two more nodes ( $f_{13}$  and  $f_{11}$ ) and in proximity of the new node ( $f_6$ ). Node  $f_{15}$  represents the variation of the number of neurites over radial direction. In the DTEG of the G93A subjects, it is now related to all the aspects of the neurite outgrowth, being connected directly or in proximity to all the morphological descriptor groups. This means that a variation in the neurite number moving away from the center of the soma can be used to discriminate healthy and unhealthy cells, being directly related to the neurite degeneration process.

### Time-dependent motor neuron evolution discrimination capability

Timing plays a crucial role in the understanding of ALS progression. To quantitatively prove this assumption, we demonstrated that TE descriptors were significant in discriminating WT motor neurons at the 6<sup>th</sup> and 8<sup>th</sup> days. We did the same for G93A motor neurons. Applying the same procedure as described before for the ALS diagnosis, but on the WT and G93A motor neurons separately, and selecting features more related to the temporal evolution process, the classification model achieved the accuracy values shown in Figure 8. It can be noted that the results are very promising and demonstrated the existence of a specific temporal pattern for the motor neurons, independent from the biological condition.

### Temporal TE graph

As a further demonstration that temporal evolution plays a role in the investigation of ALS and that there are some characteristics patterns in motor neurons according to the time of

observation, in Figure 9 we compared the temporal TE graphs of WT (left) and G93A (right) for the evolution from the 6<sup>th</sup> to 8<sup>th</sup> days of observation. Once more, we observe some intrinsic topological structure for each situation along with the additional relationship established by the specific biological/temporal condition.

### Comparative analysis with standard segmentation approaches

SS demonstrated to be a powerful approach for the automatic segmentation of motor neurons, especially with the introduction of the adaptation procedure. However, it belongs to the category of supervised segmentation approaches requiring a training procedure for the optimal network configuration. Therefore, to additionally prove the strength of such approach, we compared the performance of standard alternative segmentation methods, such as the Canny edge detection<sup>45</sup> and K-means clustering segmentation approaches.<sup>46</sup> Each of the two approaches is optimized on the labeled set of images with a motor neuron. In particular, for Canny edge detection we optimized the high threshold value,  $th_{high}$ , and the  $\sigma$  of the derivative of Gaussian filter for smoothing,<sup>45</sup> whereas for the K-means clustering approach, we optimized the number of clusters for the clustering.<sup>47</sup> Note that the algorithms are optimized for each frame so that it would be very difficult to have a system with general capability to segment any additional images, such as that provided by the ASS method. Performance were assessed through  $FM$ ,  $R$ , and  $P$  and are shown in Figure 10. Figure 10B illustrates the boxplots of the three metrics for the two approaches and Figure 10A shows an example of segmentation result for the two comparative approaches with respect to the proposed ASS method. The results achieved for the frames acquired on the 6<sup>th</sup> and 8<sup>th</sup> days are aggregated. From the observation of Figure 10, we can note that the SS approach presents some crucial peculiarities. First of all, as observed in Figure 10A, there are very few missing pixels (the so-called FN regions), represented by the purple points. This aspect is confirmed by the high value of  $R$  for the SS approach. Such a high recall value, conjugated with a moderate precision value, indicates that the segmented motor neuron generally includes the GT motor neuron labeled by the expert. It is crucial to underline the fact that over-segmentation effects related to moderate values of  $P$  mostly refer to an isotropic dilation of the motor neuron area and less frequently deal with a complete loss of area of neurites. This is a fundamental aspect in light of the further morphological characterization. In fact, the descriptors extracted after segmentation are strongly influenced by the complete representation of the motor neuron shape and would not be so significant (and above all their relationship), if the segmentation result would lose parts of the neurites. This is instead what happened, on average, with the two comparative approaches, which exhibit a very poor recall, leading to an overall  $FM$  that is comparable (Canny) and lower (K-means) with respect to the proposed approach. In addition, it can also be observed that the dispersion of the metrics calculated over the 150 training frames in the ASS approach is much smaller than that of the two comparative approaches, indicating increasing robustness and generalization capability.



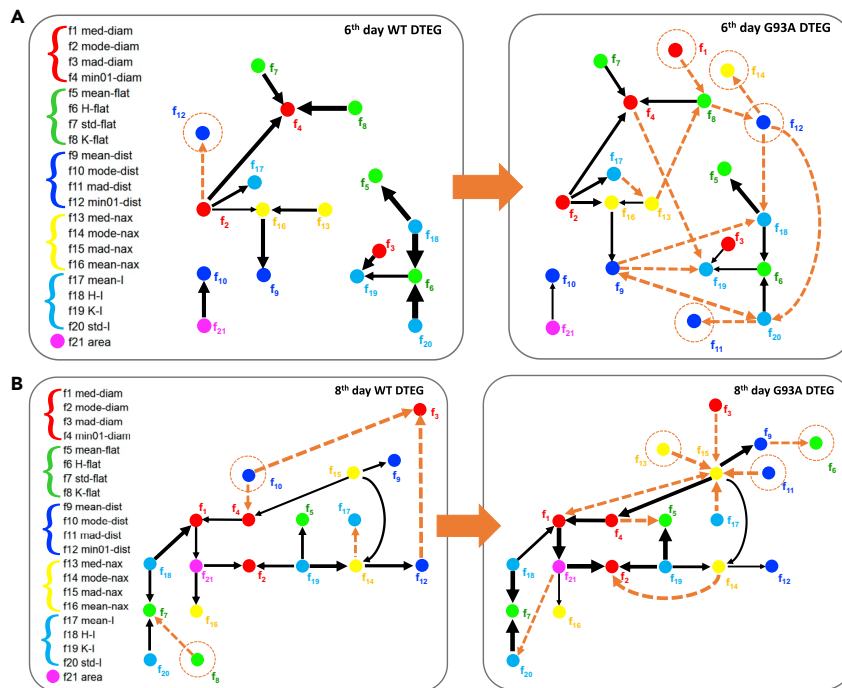


**Figure 7. Disease transfer entropy graph (DTEG)**

Disease transfer entropy graph (DTEG) for the 6<sup>th</sup>-day (A) and 8<sup>th</sup>-day (B) experiments. Solid black lines represent the subgraphs in common in the two cases (WT and G93A). The orange dotted lines identify the subgraphs specific for each specific condition (left) WT and (right) G93A. Colors represent feature groups as indicated in the legend to the left: neurites' thickness and flatness,  $f_1$ – $f_4$  (red) and  $f_5$ – $f_8$  (green), respectively; heterogeneous and global neurites extension and numerosity,  $f_9$ – $f_{12}$  (blue), and  $f_{13}$ – $f_{16}$  (yellow),  $f_{21}$  (magenta), respectively; alteration on general aspects,  $f_{17}$ – $f_{20}$  (cyan). Dashed circles represent new nodes included in the additional subgraphs.

confirmed that the *DP* of those comparative metrics is still lower than that of TE-f.

#### TE graph for treated versus untreated PC3

The TE descriptors selected for the scope of classification represent directed relationships between time-varying morphological and textual characteristics of moving PC3, highlighting

#### Performance of comparison among correlation measures, TE, and morphological descriptors

The use of TE descriptors demonstrated to be a valid tool to quantitatively represent the synergy among morphological descriptors and to be further used in discrimination procedures. TE allows transducing all of the descriptor signals of a motor neuron into a single matrix (time is collapsed) by enhancing the capacity of the descriptor signals to mutually transfer information among each other. TE is therefore capable to put in evidence and reveal if there is an ongoing dynamic process (degeneration, apoptosis, etc.) that creates an infrastructure among the geometrical and the intensity descriptors.

Furthermore, TE descriptors not only allowed representing the synergy but also the relationship, permitting to achieve a graph representation as the DTEGs shown before. However, to prove the relevance of TE descriptors for the discrimination task, we calculated additional mutual correlation metrics between the morphological features, such as the Pearson's coefficient ( $\rho_c$ ) and the concordance correlation coefficient ( $\rho_{cc}$ ).<sup>48</sup> The lack of directionality of such descriptor (i.e.,  $\rho_{cc}(i,j) = \rho_{cc}(j,i)$  by definition) led to a reduced number of features equal to 210. Figure 11 compares the most relevant descriptors from TE-fs,  $\rho_c$ -f, and  $\rho_{cc}$ -f having a *DP* higher than 0.7.

Color information is indicated in the legend. We can observe that the Pearson's coefficient features,  $\rho_c$ -f, exhibited a general lower discrimination power with only one descriptor per both days with a *DP* higher than 0.75. On the other hand,  $\rho_{cc}$ -f exhibited almost comparative *DP* values in the 8<sup>th</sup>-day experiment (only one TE-f is definitively higher than the others, with a *DP* of about 0.83), but globally reached lower *DP* values in the 6<sup>th</sup>-day experiment with only one descriptor with a *DP* higher than 0.75. Therefore, beyond the always important absence of causal relationship of the correlation metrics, we

logical and textual characteristics of moving PC3, highlighting the relationship between block replication effects induced by etoposide into dynamic phenotype alterations. A fascinating way to visually represent such relationships can be the use of a TE graph (TEG). After a restricted number of TE-fs are selected according to the *DP* value, we constructed the TEG. The TEG contains as many nodes as the number of individual descriptors involved in at least one selected mutual relationship and as many edges as the non-zero entries of the MUTE matrix for the TE-f selected. Calculating a separate TEG for untreated and treated PC3 cells, we are able to visually represent the overall relationship of descriptors extracted over the two categories. To provide the reader with this further tool, we show in Figure 12, the TEGs for untreated (Figure 12A) and treated (Figure 12B) cells, respectively. We assigned the same color to the same feature group to simplify the interpretation as indicated in the legend. The solid black edges identify the subgraphs that are in common for the two conditions. Conversely, for each category of cells, the dashed orange edges identify the subgraphs additionally present and related to the specific condition (i.e., left, untreated; right, treated). The dashed orange circles also identify nodes that are also specific for each group of subjects, due to the addition of at least one more edge.

From the comparison of the TEG in Figures 12A and 12B, it emerges that, in the treated PC3, there are more connections than in the untreated cells. In this case, it seems that more relationships appear among the descriptors. In particular, Haralick descriptors ( $f_{11}$ – $f_{14}$ ) appear to be fundamental in treated cells since three more nodes,  $f_{11}$ ,  $f_{12}$ , and  $f_{14}$  are added and linked to each other. In addition, a reinforced link is established among intensity descriptors (see edges connecting nodes  $f_9$  with nodes  $f_7$  and  $f_{10}$ ) and more importantly among Haralick features ( $f_{11}$  and  $f_{14}$ ) and shape descriptors ( $f_3$  and  $f_2$ , respectively). The latter

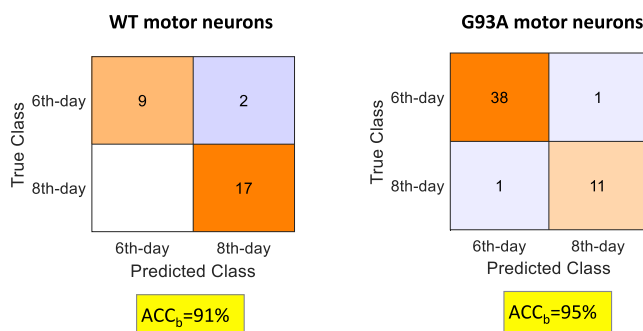


**Figure 8. Accuracy results**

Confusion matrices of the two-class problems of discriminating temporal evolution in (left) WT and (right) G93A motor neurons.

relationship is a further demonstration of the relationship between cell appearance and cell shape in treated cells.

### Comments about results, implications in future investigation, and possible extension

Although, cultured primary neurons and neurons inhabiting the brain are by definition different, and the results obtained from primary cultures cannot be directly related to an “*in vivo*” situations, they allow us to evaluate in a rather simple context the intrinsic weaknesses of specific cellular subpopulations. One obvious advantage in using dissociated neuronal cultures is decreasing the complications that result from the network properties of the brain, and so gaining a more direct access to the biology of individual neurons and eventually helping the comprehension of molecular and cellular mechanisms affecting the pathogenesis of complex neurodegenerative diseases, such as ALS. Live imaging of “*in vitro*” cellular growth and interaction mode gives the ability to directly monitor and quantify whether and how pathological conditions or pharmacological/drug treatments are capable of altering cellular movements. Cellular movements are important functional features. Interaction between cells is governed by contact and interacting molecules that guide and determine the mode and extent of communication between cells. As such, measurement of their interactions has relevance to both basic and translational research. At the same time, accurate measurements of cellular movements and intercellular contacts are challenging and this could be a difficult obstacle to overcome. Neuronal tissues comprise a remarkable number of heterogeneous cell types, at the molecular as well as at the phenotypic and morphological levels. This amazing cellular multiplicity enables the different brain areas to properly function while forming a well-connected and performing network. A question we have tried to address in this paper is: can we automatically measure through LFI the amount of modifications a diseased motor neuron shows in its movements/interaction with respect to its surrounding environment? It has long been known that cellular communication is essential for the proper homeostasis of a cell. How do cellular diversity, and cell-cell interactions and intercellular communication, work in concert to determine the proper wiring of a brain? It is now clear that the neurodegeneration problem is not merely a cell problem, it is a problem of cell interaction and intercellular communication

with distant cells and with other tissues. We know that, in many neurodegenerative diseases, including ALS, the diseased cells release, into the surrounding environment, toxic factors (mutated proteins) that can “infect” neighboring cells and spread the disease. In actual fact, it is hypothesized that neurodegenerative diseases could be considered a type of prion disease, with spreading capabilities.

In this paper, we have presented a mathematical framework that can model how a given neuron “occupies” an area by shuffling its projections and thus how it is able to keep contacts with its surrounding environment. Keeping in mind that a cell’s traveling can be heavily influenced by neighboring cells and microenvironmental factors, on top of genotypically altered features (i.e., the presence of a mutant gene), we have elaborated a series of functions that allow the interpretation of the cellular changes/movements over time (i.e., time in culture). We have observed a statistically significant increase in all the paradigms indicative of an increased stationarity in the mutant motor neurons analyzed compared with the controls. The combination of all the indexes point to an ailing motor neuron that appears less prone to develop a proper network, probably because of intrinsic (i.e., mutant gene overexpression) and extrinsic (release of mutant proteins and toxic substances by the neurons themselves and the astrocytes) factors that are realistically altering the extracellular milieu, the intracellular homeostasis, as well as the cellular membrane external signaling molecules that participate in the proper formation and wiring of the neuronal network.

It is fundamental to strengthen that the proposed approach is not only capable to recognize patterns in ALS motor neuron phenotype and its dynamical progression, but also to propose novel paradigms for the dynamical modeling of evolving biological systems. Not straightforwardly, many different systems, biological or not, manifest peculiarity not in their static assessment, but rather in the way they change over time. For this reason, we believe that the strategies presented in this paper, going from ASS to TE and related disease graph representation, are totally general and may offer to data scientists hints for improving dynamic system understanding, monitoring, and control.

The use of two distinct case studies demonstrated the adaptability of NeuTiTES to different scenarios within LFI. Although not exhaustively demonstrated in the paper, NeuTiTES can be applied to very diverse applicative contexts, going from anisotropic and ramified motor neurons to circular cancer cells with smoothed boundaries. The possibility to feed the network with manually segmented cells, in place of applying invasive staining procedure, and the expansion of the dataset of images for training, will allow us to collect a battery of semantic networks each for a specific applications, avoiding in future retraining over specific applications.

### Limitations of the study

In the present release of NeuTiTES, the preprocessing image algorithms are specifically designed for bright-field time-lapse microscopy imaging. In the future, NeuTiTES could be adapted to a wider class of optical imaging techniques, such as phase contrast imaging and fluorescence time-lapse microscopy imaging.



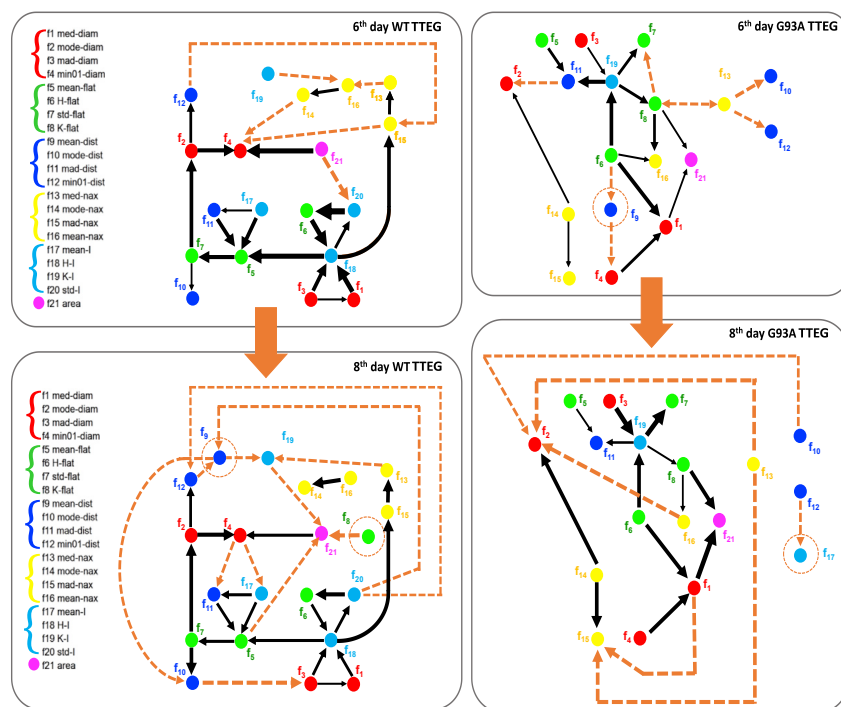


**Figure 9. Temporal transfer entropy graph (TTEG)**

Temporal transfer entropy graph (TTEG) for the 6<sup>th</sup>-day (A) and the 8<sup>th</sup>-day (B) day experiments, in representing the temporal evolution of the neurites. Solid black lines represent the subgraphs in common in the two cases (WT and G93A). The orange dotted lines identify the subgraphs specific for each specific condition (left) WT and (right) G93A. Colors represent feature groups as indicated in the legend to the left: neurites' thickness and flatness,  $f_1$ – $f_4$  (red) and  $f_5$ – $f_8$  (green) respectively; heterogeneous and global neurites extension and numerosity,  $f_9$ – $f_{12}$  (blue),  $f_{13}$ – $f_{16}$  (yellow), and  $f_{21}$  (magenta), respectively; alteration on general aspects,  $f_{17}$ – $f_{20}$  (cyan). Dashed circles represent new nodes included in the specific subgraphs.

Despite the very strong biological implication of the presented case studies, the strength of the proposed method is its intrinsic wide generalization. Actually, the new paradigm based on the idea of adapting static analysis to a dynamic context, as well as on the introduction of TE as a measure of the temporal relationship among descriptors, can be applied to many different evolving processes to improve

In the current release, NeurITES does not provide an optimal visualization of the DTEG associated with the experiment. The user is asked to design their own optimal DTEG according to the result of the thresholded TE matrix. Future releases will include an additional module for the construction and the visual optimization of the DTEG representation.

Regarding the biological aspects of the ALS study, the approach has two main limitations: the use of a mixed culture system, without a physical separation between the neuronal and the glial components, and the absence of a clear neuronal marker. In the future, by employing custom-made culture devices allowing the separate growth and select contact between the neuronal and the glial components, and by employing GFP-tagged neurons, we will be able to characterize better the interaction between neurons and eventually between neurons and glial cells.

## Conclusion

Here, we present a novel tool, NeurITES, for the automatic investigation of the dynamic processes involved in biological evolving systems. The algorithms presented in the tool aim to provide a representation model of the underlying phenomenon through the quantitative assessment of the phenotypical evolution of cell morphology over time. The application of the proposed framework to ALS research might be a complementary tool in a systematic approach for determining treatment strategies. Furthermore, this model might help in testing the effect of a drugable compound by analyzing the spatiotemporal mechanisms of neurodegenerative heterogeneity. Preliminary results are also presented for a second case study involved in investigating phenotypical alterations in prostate cancer cells under chemotherapeutic treatment.

the capacity to monitor the state but also to predict the evolution of the phenomenon. This is crucial when the understanding of the processes is not simply the collection of static conditions, but rather the variability of their mutual interaction over time.

## EXPERIMENTAL PROCEDURES

### Resource availability

#### Lead contact

The lead contact is Prof. Eugenio Martinelli, [martinelli@ing.uniroma2.it](mailto:martinelli@ing.uniroma2.it).

#### Materials availability

The videos used in this paper can be obtained on request to {martinelli, mencattini}@ing.uniroma2.it.

#### Data and code availability

All MATLAB codes and videos associated with this paper can be freely accessed and downloaded via <https://cloudstore.bee.uniroma2.it/index.php/s/eGaeonyFZg95Wf8>, password: SLA\_Patterns.

MATLAB codes can be also downloaded at: <https://github.com/Arianna1974/NeurITES.git>.

### Implementation details

According to expert opinion, and by virtue of the visual observation of the videos, motor neurons present very low motility at 1 frame/min. According to these *a posteriori* considerations, we decided to reduce the frame rate of the videos to 0.2 frame/min. This setting also reduced the memory storage of the entire video sequence (see Table 3).

In addition to the temporal resolution reduction, the frames were further spatially downsampled by a factor of two to 0.66  $\mu\text{m}/\text{px}$ . The intrinsic dimensions of motor neurons as well as the level of details that are visible in bright-field modality did not motivate the use of the setting 0.33  $\mu\text{m}/\text{px}$ , previously used for detection of prostate cancer cells.<sup>31</sup>

Experiments were run on a PC Dell G5 15, with an Intel (R) core i7-9750H, CPU @ 2.60 GHz Processor, 16 GB RAM, Windows 10 Professional 64 bits, MATLAB 2020b. Table 3 lists the computational overhead of each step in the NeurITES platform and related memory storage for a single motor neuron sequence using the described settings.

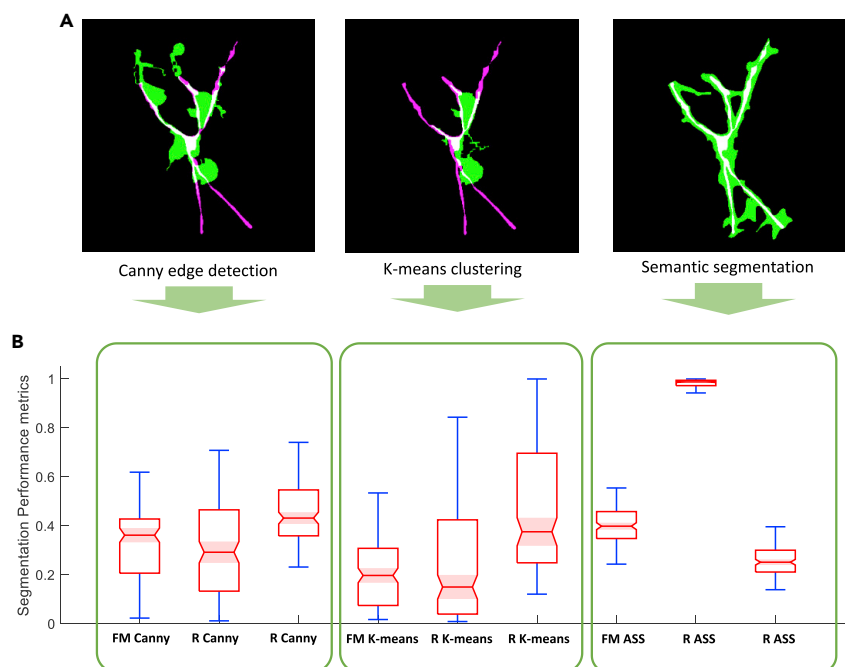


**Figure 10. Comparative segmentation results**

(A) Examples of the segmentation results obtained using Canny edge detection (left), K-means clustering (middle), and semantic segmentation (right). White pixels represent the true positive regions, green pixels represent the false positive regions (over-segmentation), and purple pixels locate the false negative regions (under-segmentation or missing regions).

(B) Segmentation metrics in terms of  $FM$ ,  $R$ , and  $P$  for the three compared approaches (Canny edge detection, K-means clustering, and ASS).

**Mouse model, cell culture, and sample preparation for the motor neuron case study:** TgN (SOD1-G93A)1Gur mice expressing the G93A mutant SOD1 (G93A) originally obtained from The Jackson Laboratory (Bar Harbor, ME, USA) are housed and bred in the C57BL/6J background at the Fondazione Santa Lucia animal facilities. For the primary cultures, a male mouse carrying the mutant SOD1G93A gene was mated with a C57BL/6J female to obtain mixed embryos, processed separately, and then screened for the presence of the human transgene.<sup>49</sup> Motor neuron cultures were divided into two groups: transgenic mutant G93A and their corresponding non-transgenic littermates (WT), which were used as controls. Animal care and use followed the European Directive 2010/63/EU adopted by the Council of the European Union for animal experiments, and adequate measures were taken to minimize pain or discomfort. The experimental protocol was approved by the Italian Ministry of Health (license no. 424/2019-PR).

Spinal cord MN-enriched cultures were prepared from 14-day-old SOD1G93A.<sup>49</sup> Each neural tube was dissected, singularly incubated for 10

min in 0.025% trypsin, and gently dissociated. The resulting mixed cultures were seeded on poly-D-lysine-coated dishes (about  $70 \times 10^4$  cells for each glass coverslip) and maintained in neurobasal medium supplemented with B-27 supplement, 0.5 mM glutamine, 5% fetal bovine serum (FBS), and 5% horse serum. Cultures were maintained in a 37°C humidified incubator in 5% CO<sub>2</sub> atmosphere. To suppress glia proliferation, at 3 days after seeding Ara-C was added to a final concentration of 10  $\mu$ M.

**Cell culture and sample preparation for the PC3 case study:** human PC3 (ATCC, Rockwell, MD) were grown at 37°C with 5% CO<sub>2</sub> in RPMI 1640 medium,

supplemented with 10% FBS, 1% L-glutamine (2 mg/mL), and 1% penicillin/streptomycin (100 IU/mL) (Euroclone). PC3 are metastatic neoplastic cells representing highly aggressive tumor cell phenotypes. Cells were treated with the chemotherapy agent etoposide at a concentration equal to 5  $\mu$ M. PC3 were also acquired under control conditions (i.e., no drug).

## Imaging and image analysis

### Time-lapse microscopy image acquisition

A customized microscope was used<sup>31</sup>: the prototype consisted of a small-scale inverted microscope suitable to work in high-humidity environments (incubators) with factory standard optics, custom aluminum structure, and fully sealed electronics. The whole-microscope dimensions were less than 400 mm in height and 350 mm in length and depth. Furthermore, a custom firmware was implemented in the MATLAB2017a environment to have full control on acquisition methods and light exposure. For case study 1, acquisition was at 1 frame/min, with 1 day of total experiment time for two different sessions (at the 6<sup>th</sup> and 8<sup>th</sup> days). For case study 2, acquisition was at 1 frame/min, for a total duration of 6 h. The captured images had a field-of-view of 1.2 mm width by 1 mm height, and a spatial resolution of 0.33  $\mu$ m/px.

**Cell segmentation using ASS:** SS is aimed at assigning labels to every pixel in a given image using deep CNNs.<sup>35</sup> In particular, in this work we implemented the DeepLabv3+,<sup>35</sup> which is based on an encoder-decoder architectures with atrous deconvolution required to re-dilate the image after pooling. The SS we implement is based on the well-assessed pretrained CNN, i.e., ResNET50.<sup>34</sup> Such a modification with respect to the default setting (ResNET18) was justified by an increase in the final performance. SS is usually applied to static images with the task of object segmentation and does not rely on video sequence segmentation. In our work, we extend the potential of SS by the ASS approach. Using ASS we not only segment the motor neuron in each video frame but adapt the general contrast of the actual frame to that of the previous one, with the aim to increase the stationarity of the segmentation results along time. The small set of manually segmented motor neurons is a limiting factor for the machine learning model's accuracy and may cause overfit to the training sample and lack of generalizability. To address this aspect, we applied an augmentation procedure aimed at artificially increasing the dataset of training by randomly rotating the images with an angle in [0,360] degrees, reflecting images, translating images up to 10 px in both directions horizontally and vertically.

After the SS network was trained on the 150 frames labeled, all the frames of the 79 videos were processed through the use of the ASS approach. In the ASS

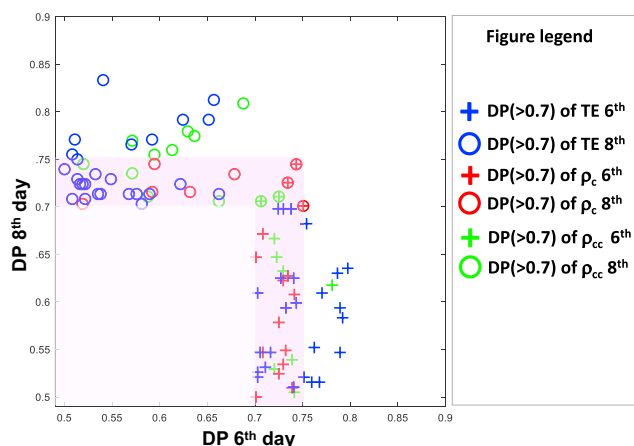


**Figure 11. DP of the compared correlation metrics**

Pearson correlation coefficient,  $\rho_c$ , concordance correlation coefficient,  $\rho_{cc}$ , and TE.

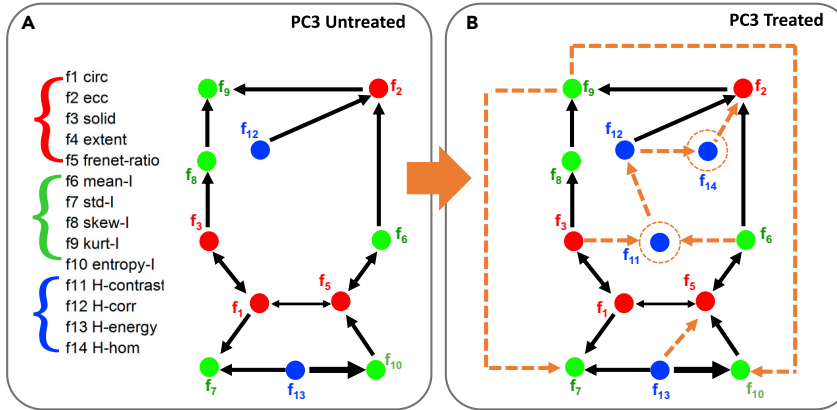


**Figure 12. Treatment transfer entropy graph (TEG)**

TTEG for the (A) the untreated PC3 cells and (B) PC3 cells treated with etoposide, a block replication drug. Solid black lines represent the subgraphs in common in the two cases. The orange dotted lines identify the subgraphs specific for each specific condition. Colors represent feature groups as indicated in the legend to the left: cell shape descriptors,  $f_1$ – $f_5$  (red); cell intensity descriptors,  $f_6$ – $f_{10}$  (green); and Haralick textural descriptors,  $f_{11}$ – $f_{14}$  (blue). Dashed circles represent new nodes included in the specific subgraphs.

application, frame contrast enhancement through nonlinear histogram stretching is repeatedly applied as follows  $I_E(x, y, t) = G(I(x, y, t))$

$$\text{with } G = \begin{cases} \left( \frac{I(x, y, t) - I_{low}}{I_{high} - I_{low}} \right)^\gamma, & \text{if } I_{low} \leq I(x, y, t) \leq I_{high} \\ 0, & \text{otherwise} \end{cases}$$

where  $I_{low} = \text{quantile}(I(x, y, t), 0.01)$  and  $I_{high} = \text{quantile}(I(x, y, t), 0.99)$  and  $\gamma$  the nonlinearity parameter of the stretching operator. In the present experiment, we changed the value of  $\gamma$  in the range [0.5–1.5]. For each  $\gamma$  value, the SS was applied to the enhanced frame and the result was compared with the segmentation result of the previous frame, by computing the FM value (see Equation 1). The result with the highest FM value was then kept as the optimal segmentation result for that frame.

### Morphological descriptors extraction for case study 1

Each segmentation mask was then used to extract morphological descriptors for each motor neuron along the video sequence. Descriptors were divided into six groups: *thickness of neurites*, *flatness of neurites* (calculated along the normal direction to the neurite), *extension of neurites* (calculated with respect to the motor neuron centroid), *number of neurites* on concentric radial region from the centroid, *pixel intensity of the neurite's soma*, and *area of the neurite's soma*. Each group, except for the last one, was coded into four distinct statistical features representing average values and variations. More specifically, the extracted features were:

- **Group1** ( $f_1$ – $f_4$ )  $\rightarrow f_1$ , median of the neurites diameter;  $f_2$ , modal value of the neurites diameter;  $f_3$ , median absolute deviation of the neurites diameter;  $f_4$ , 10<sup>th</sup> percentile of the neurite diameter.
- **Group2** ( $f_5$ – $f_8$ )  $\rightarrow f_5$ , mean value of the neurites's flatness;  $f_6$ , entropy of the neurite's flatness;  $f_7$ , standard deviation of the neurite's flatness;  $f_8$ , kurtosis of the neurite's flatness.
- **Group3** ( $f_9$ – $f_{12}$ )  $\rightarrow f_9$ , mean value of the neurites's extension;  $f_{10}$ , modal value of the neurite's extension;  $f_{11}$ , median absolute value of the neurite's extension;  $f_{12}$ , 10<sup>th</sup> percentile of the neurite's extension.
- **Group4** ( $f_{13}$ – $f_{16}$ )  $\rightarrow f_{13}$ , median value of the number of neurites;  $f_{14}$ , modal value of the number of neurites;  $f_{15}$ , median absolute value of the number of neurites;  $f_{16}$ , mean value of the number of neurites.
- **Group5** ( $f_{17}$ – $f_{20}$ )  $\rightarrow f_{17}$ , mean value of the pixel intensity in the neurite's soma;  $f_{18}$ , entropy of the pixel intensity in the neurite's soma;  $f_{19}$ , kurtosis of the pixel intensity in the neurite's soma;  $f_{20}$ , standard deviation of the pixel intensity in the neurite's soma.
- **Group6** ( $f_{21}$ )  $\rightarrow$  area of the neurite's soma.

### Morphological and textural descriptors extraction for case study 2

Each segmentation mask was then used to extract morphological and textural descriptors for each PC3 cell along the ROI sequence. Descriptors were

divided into three groups: *shape of the cell*, *pixel intensity of the cell*, and *texture descriptors inside the cell*. Each group, except for the last one, was coded into four distinct statistical features representing average values and variations. More specifically, the extracted features were:

- **Group1** ( $f_1$ – $f_5$ )  $\rightarrow f_1$ , circularity of the cell;  $f_2$ , eccentricity of the cell;  $f_3$ , solidity of the cell;  $f_4$ , convexity of the cell (extent);  $f_5$ , Frenet ratio.
- **Group2** ( $f_6$ – $f_{10}$ )  $\rightarrow f_6$ , mean value of the cell intensity;  $f_7$ , standard deviation of the cell intensity;  $f_8$ , skewness of the cell intensity;  $f_9$ , kurtosis of the cell intensity;  $f_{10}$ , entropy of the cell intensity.
- **Group3** ( $f_{11}$ – $f_{14}$ )  $\rightarrow f_{11}$ , Haralick contrast of the cell;  $f_{12}$ , Haralick correlation of the cell;  $f_{13}$ , Haralick energy of the cell;  $f_{14}$ , Haralick homogeneity of the cell.

For the detailed description of the Haralick parameters computation, see Haralick and Shapiro.<sup>44</sup>

### TE-f calculation

Each descriptor  $f_i$  was calculated at each time frame and led to the definition of a time series,  $f_i(t)$ ,  $i = 1, \dots, N_f$ , with  $N_f$  the number of descriptors. Due to the acquisition process, each time series could be represented by a so-called stochastic process. We were interested in evaluating the information flow from the source system  $X = f_i(t)$  to the destination system  $Y = f_j(t)$ ,  $i \neq j$ . The directed transfer of information between  $X$  and  $Y$  is then linked to the measure of the directed relationship. Since the signature of causality involves at least three variables,<sup>50,51</sup> the computation of TE between  $X$  and  $Y$  requires to collect the remaining processes in the vector  $\mathbf{Z} = \{f_q(t)\}$ , with  $q \neq \{i, j\}$ . Such a framework was developed under the assumption of stationarity, which allowed to perform estimations replacing ensemble averages with time averages. By sampling the processes,  $X$ ,  $Y$ , and  $\mathbf{Z}$  at time  $t = n$ , we obtained the process observation,  $X_n$ ,  $Y_n$ , and  $\mathbf{Z}_n$ . In addition, we denoted with  $X_n^- = \{X_{n-1}, X_{n-2}, \dots\}$ ,  $Y_n^- = \{Y_{n-1}, Y_{n-2}, \dots\}$ , and  $\mathbf{Z}_n^- = \{\mathbf{Z}_{n-1}, \mathbf{Z}_{n-2}, \dots\}$  the collection of the past of the processes. Then, the MUTE from  $X$  to  $Y$  conditioned to  $\mathbf{Z}$  was defined as:

$$TE_{X \rightarrow Y | \mathbf{Z}} = \sum p(Y_n | Y_n^-, X_n, X_n^-, \mathbf{Z}_n) \log \frac{p(Y_n | Y_n^-, X_n, X_n^-, \mathbf{Z}_n)}{p(Y_n | Y_n^-, \mathbf{Z}_n)}, \quad (\text{Equation 3})$$

Where the sum extends over all the points forming the time series,  $p(u)$  is the probability associated to the variable  $u$  and  $p(u|v) = p(u, v)/p(v)$  (Bayes's theorem)<sup>52</sup> is the probability of observing  $u$  knowing the values of  $v$ . The TE measures the information explained by the past of the process  $X$  on the present of the process  $Y$  that is not already provided by the past of  $Y$  or any other process included in  $\mathbf{Z}$ . The TE could be formulated also as the difference of two conditional Shannon entropies ( $H$ ) as follows:

$$TE_{X \rightarrow Y | \mathbf{Z}} = H(Y_n | Y_n^-, \mathbf{Z}_n^-) - H(Y_n | Y_n^-, X_n^-, \mathbf{Z}_n^-), \quad (\text{Equation 4})$$

where the first term only accounts for the individual predictiveness of the output process  $Y$ , whereas the second term accounts for the cross-predictiveness of  $X$  over  $Y$ .

TE did not assume any probabilistic model for the interaction between the systems and it was able to discover nonlinear interactions over different delays. TE was implemented using the MUTE toolbox.<sup>30</sup> Starting from  $N_t$  time series for the morphological descriptors, the TE calculation led to a matrix of  $N_t \times N_t$  elements, in which the general element  $TE-f(i,j)$  represented the interaction in terms of predictiveness of  $X = f_i(t)$  and  $Y = f_j(t)$  after setting the remaining descriptors  $f_q(t)$ ,  $q \neq \{i,j\}$ , in the conditioned term  $Z$ . It was important to note that the TE-f matrix is not symmetric since a time series-directed relationship is an intrinsic asymmetric phenomenon. By turning the TE-f matrix into a vector of TE descriptors, and eliminating the diagonal elements (which are forced to be zero by definition), we obtained a TE-descriptor vector of  $N_t \times (N_t - 1)$  elements. In the two case studies considered, we have for case study 1  $N_t = 21$ , hence 420 TE descriptors, and for case study 2  $N_t = 14$ , hence 182 TE descriptors.

### Classification model construction

The TE descriptor vector is then used for constructing a classification model using linear discriminant analysis.<sup>46</sup> The descriptors were reduced by applying a *DP*-based feature selection procedure, keeping only descriptors with *DP* larger than 0.7. The selection was performed in the cross-validation loop using a LOMO procedure for case study 1 and a leave-one-track-out procedure for case study 2. Each motor neuron was finally labeled with the category of healthy (WT) or unhealthy (G93A), whereas each PC3 track was labeled as untreated or treated.

### AUTHOR CONTRIBUTIONS

Conceptualization, A.M., E.M., P.L., and A.S.; methodology, A.M., E.M., P.L., A.S., and P.C.; formal analysis, A.M. and E.M.; investigation, A.S., M.C.C., J.F., F.C., D.D.G., and P.C.; writing – original draft, A.M., A.S., P.L., and E.M.; writing – review & editing, all authors; visualization, A.M., P.C., M.D., and G.A.; funding acquisition, P.L. and E.M.; resources, P.L. and A.S.; supervision, E.M.

### DECLARATION OF INTERESTS

The authors declare no competing interests.

Received: February 1, 2021

Revised: March 2, 2021

Accepted: April 15, 2021

Published: May 25, 2021

### REFERENCES

- Caldon, C.E., and Burgess, A. (2019). Label free, quantitative single-cell fate tracking of time-lapse movies. *MethodsX* 6, 2468–2475. <https://doi.org/10.1016/j.mex.2019.10.014>.
- Specht, E.A., Braselmann, E., and Palmer, A.E. (2017). A critical and comparative review of fluorescent tools for live-cell imaging. *Annu. Rev. Physiol.* 79, 93–117. <https://doi.org/10.1146/annurev-physiol-022516-034055>.
- Walker-Daniels, J. (2012). Live cell imaging methods review. *Mater. Methods* 2. <https://doi.org/10.13070/mm.en.2.124>.
- Jeknić, S., Kudo, T., and Covert, M.W. (2019). Techniques for studying decoding of single cell dynamics. *Front. Immunol.* 10. <https://doi.org/10.3389/fimmu.2019.00755>. eCollection 2019.
- Kasprowicz, R., Suman, R., and O'Toole, P. (2017). Characterising live cell behaviour: traditional label-free and quantitative phase imaging approaches. *Int. J. Biochem. Cell Biol.* 84, 89–95. <https://doi.org/10.1016/j.biocel.2017.01.004>.
- Thorn, K. (2016). A quick guide to light microscopy in cell biology. *Mol. Biol. Cell* 27, 219–222. <https://doi.org/10.1091/mbc.E15-02-0088>.
- Boillée, S., Vande Velde, C., and Cleveland, D.W. (2006). ALS: a disease of motor neurons and their non neuronal neighbors. *Neuron* 52, 39–59. <https://doi.org/10.1016/j.neuron.2006.09.018>.
- Le Gall, L., Anakor, E., Connolly, O., Vijayakumar, U.G., Duddy, W.J., and Duguez, S. (2020). Molecular and cellular mechanisms affected in ALS. *J. Pers. Med.* 10, E101. <https://doi.org/10.3390/jpm10030101>.
- Fischer, L.R., Culver, D.G., Tennant, P., Davis, A.A., Wang, M., Castellano-Sanchez, A., Khan, J., Polak, M.A., and Glass, J.D. (2004). Amyotrophic lateral sclerosis is a distal axonopathy: evidence in mice and man. *Exp. Neurol.* 2004, 232–240. <https://doi.org/10.1016/j.expneurol.2003.10.004>.
- Pun, S., Santos, A.F., Saxena, S., Xu, L., and Caroni, P. (2006). Selective vulnerability and pruning of phasic motoneuron axons in motoneuron disease alleviated by CNTF. *Nat. Neurosci.* 9, 408–419. <https://doi.org/10.1038/nn1653>.
- Dadon-Nachum, M., Melamed, E., and Offen, D. (2011). The “dying-back” phenomenon of motor neurons in ALS. *J. Mol. Neurosci.* 43, 470–477. <https://doi.org/10.1007/s12031-010-9467-1>.
- Ebstein, S.Y., Yagudayeva, I., and Shneider, N.A. (2019). Mutant TDP-43 causes early-stage dose-dependent motor neuron degeneration in a TARDBP knockin mouse model of ALS. *Cell Rep.* 26, 364–373.e4. <https://doi.org/10.1016/j.celrep.2018.12.045>.
- Frey, D., Schneider, C., Xu, L., Borg, J., Spooren, W., and Caroni, P. (2000). Early and selective loss of neuromuscular synapse subtypes with low sprouting competence in motoneuron diseases. *J. Neurosci.* 20, 2534–2542. <https://doi.org/10.1523/JNEUROSCI.20-07-02534.2000>.
- Clark, J.A., Southam, K.A., Blizzard, C.A., King, A.E., and Dickson, T.C. (2016). Axonal degeneration, distal collateral branching and neuromuscular junction architecture alterations occur prior to symptom onset in the SOD1(G93A) mouse model of amyotrophic lateral sclerosis. *J. Chem. Neuroanat.* 76 (Pt A), 35–47. <https://doi.org/10.1016/j.jchemneu.2016.03.003>.
- De Vos, K.J., Chapman, A.L., Tennant, M.E., Manser, C., Tudor, E.L., Lau, K.F., Brownlee, J., Ackerley, S., Shaw, P.J., McLoughlin, D.M., et al. (2007). Familial amyotrophic lateral sclerosis-linked SOD1 mutants perturb fast axonal transport to reduce axonal mitochondria content. *Hum. Mol. Genet.* 16, 2720–2728. Epub. <https://doi.org/10.1093/hmg/ddm226>.
- Moller, A., Bauer, C.S., Cohen, R.N., Webster, C.P., and De Vos, K.J. (2017). Amyotrophic lateral sclerosis-associated mutant SOD1 inhibits anterograde axonal transport of mitochondria by reducing Miro1 levels. *Hum. Mol. Genet.* 26, 4668–4679. PMID: 28973175. <https://doi.org/10.1093/hmg/ddx348>.
- Naumann, M., Pal, A., Goswami, A., Lojewski, X., Japtok, J., Vehlow, A., Naujock, M., Günther, R., Jin, M., and Stanslowsky, N. (2018). Impaired DNA damage response signaling by FUS-NLS mutations leads to neurodegeneration and FUS aggregate formation. *Nat. Commun.* 9, 335. <https://doi.org/10.1038/s41467-017-02299-1>.
- White, M.A., Lin, Z., Kim, E., Henstridge, C.M., Pena Altamira, E., Hunt, C.K., Burchill, E., Callaghan, I., Loreto, A., Brown-Wright, H., et al. (2019). Sarm1 deletion suppresses TDP-43-linked motor neuron degeneration and cortical spine loss. *Acta Neuropathol. Commun.* 7, 166. <https://doi.org/10.1186/s40478-019-0800-9>.
- Abo-Rady, M., Kalmbach, N., Pal, A., Schludi, C., Janosch, A., Richter, T., Freitag, P., Bickle, M., Kahlert, A.K., Petri, S., et al. (2020). Knocking out C9ORF72 exacerbates axonal trafficking defects associated with hexanucleotide repeat expansion and reduces levels of heat shock proteins. *Stem Cell Rep.* 14, 390–405. <https://doi.org/10.1016/j.stemcr.2020.01.010>.
- Ossinger, A., Bajic, A., Pan, S., Andersson, B., Ranefall, P., Hailer, N.P., and Schizas, N. (2020). A rapid and accurate method to quantify neurite outgrowth from cell and tissue cultures: two image analytic approaches using adaptive thresholds or machine learning. *J. Neurosci. Methods* 331, 108522. <https://doi.org/10.1016/j.jneumeth.2019.108522>.
- Meijering, E., Jacob, M., Sarria, J.-C.F., Steiner, P., Hirling, H., and Unser, M. (2004). Design and validation of a tool for neurite tracing and analysis in fluorescence microscopy images. *Cytometry A J. Int. Soc. Anal. Cytol.* 58.2, 167–176. <https://doi.org/10.1002/cyto.a.20022>.
- Pool, M., Thiemann, J., Bar-Or, A., and Fournier, A.E. (2008). NeuriteTracer: a novel ImageJ plugin for automated quantification of neurite outgrowth. *J. Neurosci. Methods* 168.1, 134–139.



23. Fanti, Z., Elena Martinez-Perez, M., and De-Miguel, F.F. (2011). Neurongrowth, a software for automatic quantification of neurite and filopodial dynamics from time-lapse sequences of digital images. *Dev. Neurobiol.* 71.10, 870–881. <https://doi.org/10.1002/dneu.20866>.
24. Narro, M.L., Yang, F., Kraft, R., Wenk, C., Efrat, A., and Restifo, L.L. (2007). NeuronMetrics: software for semi-automated processing of cultured neuron images. *Brain Res.* 1138, 57–75. <https://doi.org/10.1016/j.brainres.2006.10.094>.
25. Ho, S.Y., Chao, C.Y., Huang, H.L., Chiu, T.W., Charoenkwan, P., and Hwang, E. (2011). NeurphologyJ: an automatic neuronal morphology quantification method and its application in pharmacological discovery. *BMC Bioinformatics* 12.1, 1–18. <https://doi.org/10.1186/1471-2105-12-230>.
26. Zhang, Y., Zhou, X., Degterev, A., Lipinski, M., Adjeroh, D., Yuan, J., and Wong, S.T. (2007). Automated neurite extraction using dynamic programming for high-throughput screening of neuron-based assays. *Neuroimage* 35.4, 1502–1515. <https://doi.org/10.1016/j.neuroimage.2007.01.014>.
27. Ong, K.H., De, J., Cheng, L., Ahmed, S., and Yu, W. (2016). NeuronCyto II: an automatic and quantitative solution for crossover neural cells in high throughput screening. *Cytometry A* 89.8, 747–754. <https://doi.org/10.1002/cyto.a.22872>.
28. Torres-Espin, A., Santos, D., González-Pérez, F., del Valle, J., and Navarro, X. (2014). Neurite-J: an image-J plug-in for axonal growth analysis in organotypic cultures. *J. Neurosci. Methods* 236, 26–39. <https://doi.org/10.1016/j.jneumeth.2014.08.005>.
29. Lateef, F., and Ruichek, Y. (2019). Survey on semantic segmentation using deep learning techniques. *Neurocomputing* 338, 321–348. <https://doi.org/10.1016/j.neucom.2019.02.003>.
30. Montalto, A., Faes, L., and Marinazzo, D. (2014). MuTE: a MATLAB toolbox to compare established and novel estimators of the multivariate transfer entropy. *PLoS One* 9.10, e109462. <https://doi.org/10.1371/journal.pone.0109462>.
31. Giuseppe, D.D., Corsi, F., Mencattini, A., Comes, M.C., Casti, P., Di Natale, C., Ghibelli, L., and Martinelli, E. (2019). Learning cancer-related drug efficacy exploiting consensus in coordinated motility within cell clusters. *IEEE Trans. Biomed. Eng.* 66.10, 2882–2888. <https://doi.org/10.1109/TBME.2019.2897825>.
32. Carriedo, S.G., Yin, H.Z., and Weiss, J.H. (1996). Motor neurons are selectively vulnerable to AMPA/kainate receptor-mediated injury in vitro. *J. Neurosci.* 16, 4069–4079. <https://doi.org/10.1523/JNEUROSCI.16-13-04069>.
33. Vandenberghe, W., Robberecht, W., and Brorson, J.R. (2000). AMPA receptor calcium permeability, GluR2 expression, and selective motoneuron vulnerability. *J. Neurosci.* 20, 123–132. <https://doi.org/10.1523/JNEUROSCI.20-01-00123.2000>.
34. Senthikumar, N. and R. Rajesh. (2009) Image segmentation-a survey of soft computing approaches. 2009 International Conference on Advances in Recent Technologies in Communication and Computing. IEEE, 2009. 10.1109/ARTCom.2009.219.
35. Chen, L., Zhu, Y., Papandreou, G., Schroff, F., and Adam, H. (2018). Encoder-decoder with atrous separable convolution for semantic image segmentation. In *Computer Vision — ECCV 2018*, V. Ferrari, M. Hebert, C. Sminchisescu, and Y. Weiss, eds. (Springer), pp. 833–851.
36. He, K., X. Zhang, S. Ren, and J. Sun. (2016) Deep residual learning for image recognition. In *Proceedings of the IEEE Conference on Computer Vision and Pattern Recognition*, pp. 770–778.
37. Sholl, D.A. (1953). Dendritic organization in the neurons of the visual and motor cortices of the cat. *J. Anat.* 87, 387–406.
38. Haughton, D., Kamis, A., and Scholten, P. (2006). A review of three directed acyclic graphs software packages: MIM, Tetrad, and WinMine. *Am. Stat.* 60.3, 272–286. <https://doi.org/10.1198/000313006X117972>.
39. Gurney, M.E., Pu, H., Chiu, A.Y., Dal Canto, M.C., Polchow, C.Y., Alexander, D.D., Caliendo, J., Hentati, A., Kwon, Y.W., Deng, H.X., et al. (1994). Motor neuron degeneration in mice that express a human Cu, Zn superoxide dismutase mutation. *Science* 264, 1772–1775. <https://doi.org/10.1126/science.8209258>.
40. Collins, T.J. (2007). ImageJ for microscopy. *Biotechniques* 43, S25–S30. <https://doi.org/10.2144/000112517>.
41. Powers, D.M.W. (2020). Evaluation: from precision, recall and F-measure to ROC, informedness, markedness and correlation. *arXiv*, 37–63, [arXiv:2010.16061](https://arxiv.org/abs/2010.16061).
42. Fawcett, T. (2006). An introduction to ROC analysis. *Pattern Recognit. Lett.* 27, 861–874. <https://doi.org/10.1016/j.patrec.2005.10.010>.
43. Schreiber, T. (2000). Measuring information transfer. *Phys. Rev. Lett.* 85.2. <https://doi.org/10.1103/PhysRevLett.85.461>.
44. Haralick, R.M., and Shapiro, L.G. (1992). *Computer and Robot Vision, Vol. 1* (Addison-Wesley), p. 459.
45. Gonzalez, R.C., Eugene Woods, R., and Eddins, S.L. (2004). *Digital Image Processing Using MATLAB* (Pearson Education India).
46. Duda, R.O., Hart, P.E., and Stork, D.G. (2012). *Pattern Classification* (John Wiley & Sons).
47. Arthur, D. and S. Vassilvitskii. (2007) k-means++: The Advantages of Careful Seeding. SODA '07: Proceedings of the Eighteenth Annual ACM-SIAM Symposium on Discrete Algorithms. New Orleans, LA, 1027–1035.
48. Carrasco, J.L., and Jover, L. (2003). Estimating the generalized concordance correlation coefficient through variance components. *Biometrics* 59, 849–858. <https://doi.org/10.1111/j.0006-341X.2003.00099.x>.
49. Spalloni, A., Albo, F., Ferrari, F., Mercuri, N., Bernardi, G., Zona, C., and Longone, P. (2004). Cu/Zn-superoxide dismutase (GLY93→ALA) mutation alters AMPA receptor subunit expression and function and potentiates kainate-mediated toxicity in motor neurons in culture. *Neurobiol. Dis.* Mar. 15, 340–350. <https://doi.org/10.1016/j.nbd.2003.11.012>.
50. Pearl, J. (2009). *Causality: models, reasoning and inference*, 2nd ed. (Cambridge University Press).
51. Rebane, G., and Pearl, J. (2013). The recovery of causal poly-trees from statistical data. *arXiv*, 222–228, [arXiv:1304.2736](https://arxiv.org/abs/1304.2736).
52. Papoulis, A., and Unnikrishna Pillai, S. (2002). *Probability, Random Variables, and Stochastic Processes* (Tata McGraw-Hill Education).